J. Fluid Mech. (2024), *vol*. 999, A29, doi:10.1017/jfm.2024.683

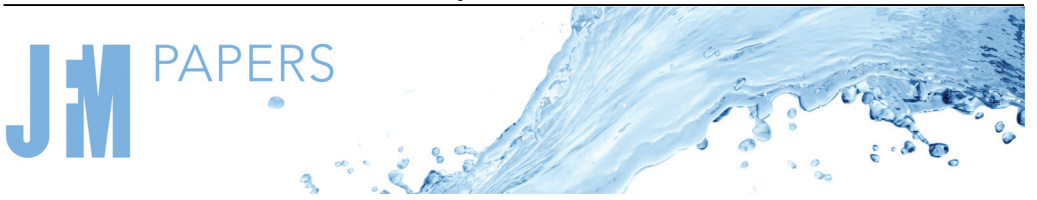

Wave turbulence in a rotating channel: numerical implementation and results

A. Eremin[1], **J.F. Scott**[1,†], **F.S. Godeferd**[1] **and A. Cadiou**[1]

[1]Ecole Centrale de Lyon, CNRS, Universite Claude Bernard Lyon 1, INSA Lyon, Laboratoire de Mécanique des Fluides et d'Acoustique (UMR5509), 36 avenue Guy de Collongue, 69134 Ecully CEDEX, France

(Received 16 November 2023; revised 13 May 2024; accepted 3 July 2024)

The analysis of Scott (*J. Fluid Mech.*, vol. 741, 2014, pp. 316–349) is implemented numerically. Decaying turbulence is confined to a channel between two infinite, parallel, rotating walls. The Rossby and Ekman numbers are supposed small, the former condition making nonlinearity small, while the latter allows the turbulence to persist for the many rotational periods needed for the small nonlinearity to be effective. The flow is expressed as a combination of inertial waveguide modes, indexed by a two-dimensional wave vector $\boldsymbol{k}$ and an integer n. The $n = 0$ modes form a two-dimensional component of the flow, whereas the remainder is the wave component, on which attention is focused in this article. Assuming statistical axisymmetry and homogeneity in directions parallel to the walls, the second-order moments of the mode amplitudes yield a spectral matrix $A_{nm}(k, t)$ (where $k = |\boldsymbol{k}|$), of which the diagonal elements describe the distribution of energy over different modes. Wave-turbulence analysis provides an equation governing the time evolution of A_{nn}, $n \neq 0$, the wave spectra, which forms the basis for the present work. The initial distribution of energy is Gaussian and depends on a parameter Ξ, the initial spectral width. The problem has two other parameters, β_w and β_v, which correspond to two distinct viscous dissipative mechanisms: wall damping due to boundary layers and volumetric damping by viscous effects throughout the flow. Results obtained by numerical solution include the time evolution of the total wave energy, E, and the detailed description of its distribution over k and n provided by $A_{nn}(k)$.

Key words: rotating turbulence, wave-turbulence interactions, homogeneous turbulence

1. Introduction

The spectral theory of homogeneous turbulence without boundaries dates back a long way (see e.g. the book by Batchelor 1953), while more recent studies have allowed for effects

† Email address for correspondence: julian.scott@ec-lyon.fr

such as rotation and stratification which tend to produce anisotropy. The understanding of turbulence in the presence of rotation is a basic problem of fluid mechanics, whose applications include geophysical flows, turbomachinery and astrophysics. In the geophysical context, we refer the reader to the reviews by Moum (2021), Fritts & Alexander (2003), Kim, Eckermann & Chun (2003) and Thomas (2023). We also refer the reader to the book by Sagaut & Cambon (2018) for a wide-ranging discussion of work on homogeneous turbulence, in particular chapter 7, which concerns turbulence with rotation.

Among the many approaches which have previously been used to attack the problem of rotating turbulence, spectral closures bear a close relationship to the present work. In particular, the EDQNM (eddy damped quasi-Markovian) model has been the subject of articles by Cambon & Jacquin (1989), Waleffe (1993) and Cambon, Mansour & Godeferd (1997). Direct numerical simulation (DNS) has also played an increasingly important role in recent years (see e.g. Teitelbaum & Mininni 2012 and references therein). However, we should note that estimates of the computational cost of credible DNS for the present problem suggest it is well out of reach of current computational resources for the parameter regimes considered here. On the other hand, the approach used here requires a significant, but not excessive, computational effort.

There have been numerous experimental studies of rotating turbulence, of which only a few are cited here. Hopfinger, Browand & Gagne (1982) used a rotating tank to quantify turbulence forced by an oscillating grid, while more recent studies of decaying turbulence (so more closely related to the problem considered here) by Morize, Moisy & Rabaud (2005) and Staplehurst, Davidson & Dalziel (2008) measured spectra and higher-order moments. Morize & Moisy (2006) is notable in the present context because they specifically discuss the effects of confinement (free surface at the top and solid at the bottom). Monsalve *et al.* (2020) is also relevant because, although they consider the forced case, their study is set within and analysed in the context of wave-turbulence theory.

Wave-turbulence theory (see Zakharov, L'vov & Falkovich 1992; Nazarenko 2011; Newell & Rumpf 2011) is a natural choice for weak turbulence, i.e. when nonlinearity is small, meaning a small Rossby number in the case of rotating turbulence. It requires dispersive waves, such as the inertial ones which result from rotation. When the turbulence is weak, linear theory provides an approximation which is valid for time spans comparable to the wave period. However, nonlinearity can have significant effects over longer time scales and wave-turbulence theory aims to describe the long-term evolution of the turbulent energy spectra which results. An important consequence of that theory is that nonlinear interactions between different spatial Fourier components of the flow are dominated by near resonances, where resonance means that the sum of frequencies of the interacting waves is zero. The weaker the turbulence the more closely the resonance condition must be met to achieve effective interaction.

Wave-turbulence theory has been used by Galtier (2003) and Bellet *et al.* (2006) to study the evolution of unconfined, homogeneous rotating turbulence at small Rossby number. Bellet *et al.* also showed that the EDQNM model becomes wave-turbulence theory in the limit of small Rossby number and presented results of numerical integration of the wave-turbulence equations, thus extracting detailed information from the theory.

The above studies of wave turbulence suppose it unbounded and statistically homogeneous. However, turbulence is never truly without bounds and it is of interest to consider the effects of confinement. There is a considerable literature (see Kartashova 1994; Pushkarev 1999; Zakharov *et al.* 2005; Lvov, Nazarenko & Pokorni 2006; Bourouiba 2008; Nazarenko 2011, chapter 10 and references therein) on wave turbulence confined in three dimensions with comparable length scales of confinement in all directions. Such confinement implies wave modes having discrete frequencies. This makes it harder to

satisfy the condition of near resonance, increasingly so as the turbulence is weakened. As a result, nonlinear interactions are suppressed and are unimportant for sufficiently weak turbulence.

However, there is an interesting case, to which this article belongs, in which the turbulence is confined in just one or two dimensions. In that case, modal frequencies, rather than being discrete, form a continuum, so resonances can always be fully effective, although confinement may still have an effect. For instance, the turbulence may no longer be homogeneous in the direction(s) of confinement, while it remains so in the unconfined direction(s). Of course, no real system is infinite, so we have in mind one for which the confinement lengths are much longer in certain directions than in others.

In this article, as in Scott (2014) (henceforth referred to as [I]), we consider decaying, weak turbulence in an infinite, rotating channel with rotation vector perpendicular to the two infinite parallel walls which bound the channel. The aim is to construct and exploit a numerical implementation of the analysis given in [I], the work described here forming the main part of the PhD thesis of Eremin (2019). A related study is that of Godeferd & Lollini (1999), who, motivated by the experimental work of Hopfinger *et al.* (1982), give results of forced DNS for a rotating channel.

The paper is organised as follows. Section 2 describes the relevant parts of the analysis of [I]. Modes, which are solutions of the linearised, inviscid governing equations, are defined. They are distinguished by a two-dimensional (2-D) wave vector $\boldsymbol{k}$ and an integer n, the modal order. The flow is expressed as a combination of modes, the modal amplitudes, $a_n(\boldsymbol{k})$, providing a description of the flow at any given time. The turbulence is assumed statistically axisymmetric and homogeneous in directions parallel to the walls. The second-order moments of $a_n(\boldsymbol{k})$ provide a spectral matrix, $A_{nm}(k)$ (where $k = |\boldsymbol{k}|$), whose diagonal elements are referred to as spectra and express the energy distribution over $\boldsymbol{k}$ and n.

Modes are divided into two families: $n = 0$ and $n \neq 0$. The former are independent of x_3 and are thus referred to as 2-D, while the latter are called wave modes. Combining the contributions of all $n = 0$ modes gives the 2-D component of the flow, whereas the remainder is the wave component, which is the focus of this article. Assuming weak turbulence and small viscosity, wave-turbulence theory leads to an integro-differential equation which describes the time evolution of the wave spectra, $A_{nn}(k)$ $(n \neq 0)$. Extracting results using numerical solution of this equation is the objective of this article.

Finally, § 3 describes the numerical implementation of the wave-turbulence equation, while § 4 gives results.

2. Analytical basis

As noted in the introduction, the work described here is based on the analytical results of [I] concerning rotating turbulence in an infinite channel bounded by solid walls at which a no-slip condition applies. A rotating system of Cartesian coordinates, x_1, x_2, x_3, is used, where $0 < x_3 < h$ and the walls lie at $x_3 = 0$ and $x_3 = h$. The rotation vector, $\boldsymbol{\Omega} = (0, 0, \Omega)$, is perpendicular to the walls. The geometry is illustrated in figure 1. Spatial coordinates are non-dimensionalised using h and time by $(2\Omega)^{-1}$. The fluid velocity is correspondingly non-dimensionalised using $2\Omega h$. There is no mean flow in the rotating frame of reference used here and the turbulence is assumed statistically axisymmetric and homogeneous in directions parallel to the walls, as well as weak, meaning a small Rossby number, $\varepsilon = u'/(2\Omega h)$, where u' measures the turbulent velocity. Note that, at this stage, u', and hence ε, are order-of-magnitude quantities. They will later be made precise using the initial conditions.

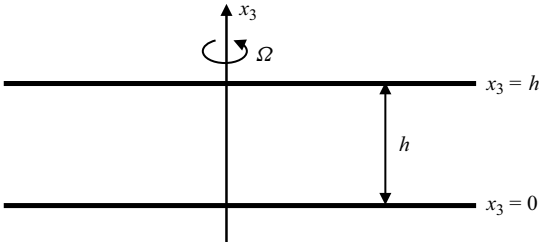

Figure 1. The problem geometry.

Assuming weak turbulence, linear theory applies over time spans of $O(1)$ (i.e. comparable to the rotational period). Unless the Ekman number, $Ek = \nu/(2\Omega h^2)$ (where ν is viscosity) is small, decay due to viscous dissipation occurs before nonlinearity can act. It is therefore supposed that the Ekman number is small, allowing the possibility of significant cumulative effects of weak nonlinearity at large t. Given weak turbulence and small dissipation, it is natural to consider the linear problem without viscosity, whose solutions are the inertial-wave modes defined in [I], § 2.1. Modes are complex solutions of the linearised, inviscid governing equations whose velocity fields have the form

$$u_i = W_i^{(n)}(x_3; \boldsymbol{k}) \exp\{\mathrm{i}k_1 x_1 + \mathrm{i}k_2 x_2 - \mathrm{i}\omega_n(k)t\}, \tag{2.1}$$

where the mode is indexed by the (2-D) wave vector $\boldsymbol{k} = (k_1, k_2)$ and the mode order n, which is an integer defining the axial structure of the mode via

$$W_1^{(n)}(x_3; \boldsymbol{k}) = \frac{k_1\omega_n(k) + \mathrm{i}k_2}{k} \cos(n\pi x_3), \tag{2.2}$$

$$W_2^{(n)}(x_3; \boldsymbol{k}) = \frac{k_2\omega_n(k) - \mathrm{i}k_1}{k} \cos(n\pi x_3), \tag{2.3}$$

$$W_3^{(n)}(x_3; \boldsymbol{k}) = -\frac{\mathrm{i}k}{(k^2 + n^2\pi^2)^{1/2}} \sin(n\pi x_3). \tag{2.4}$$

In the above equations, $k = |\boldsymbol{k}|$ is the wavenumber and

$$\omega_n(k) = \frac{n\pi}{(k^2 + n^2\pi^2)^{1/2}}, \tag{2.5}$$

is the dispersion relation, which lies in the range $|\omega_n| \leq 1$. Note that, writing $\cos(n\pi x_3)$ and $\sin(n\pi x_3)$ in terms of $\exp(\pm \mathrm{i}n\pi x_3)$, the right-hand side of (2.1) can interpreted as a combination of two plane waves, $\exp(\mathrm{i}\boldsymbol{K}_\pm \cdot \boldsymbol{x} - \mathrm{i}\omega t)$, where $\boldsymbol{K}_\pm = (k_1, k_2, \pm n\pi)$ are 3-D wave vectors and $\omega = \pm K_3/|\boldsymbol{K}|$ is the usual dispersion relation of plane inertial waves. Taking one of these waves, its wall reflection gives the other. Thus, the mode can be thought of as expressing multiple reflections of plane waves by the walls.

Modes with $n = 0$ are 2-D, having $u_3 = 0$ and no dependency on x_3. They are of zero frequency, representing steady flows in the absence of nonlinearity and viscosity. For readers acquainted with the case of combined stratification and rotation, such modes should not be confused with the 'vortical' (more precisely, 'potential vorticity' (see e.g. Müller 1995)) modes, which are often used to describe turbulence when stratification is present (see e.g. Bartello 1995; Scott & Cambon 2024 for more details). 'Vortical' modes need not be 2-D, but, like the 2-D ones of the present work, have zero frequency, hence a possible confusion. In the case of pure rotation considered here,

'vortical' modes reduce to a passive scalar, not considered here, and their contribution to the velocity field is zero. Thus, because we only consider the velocity field, 'vortical' modes do not appear in the present study. They are only needed when stratification is present.

The modes defined above form a complete set for solenoidal velocity fields, so, at any instant of time, the flow can be expressed as a linear combination of modes, even in the presence of nonlinearity and viscosity. Thus

$$u_i(\boldsymbol{x}, t) = \sum_{n=-\infty}^{\infty} \int a_n(\boldsymbol{k}, t) W_i^{(n)}(x_3; \boldsymbol{k}) \exp\{\mathrm{i}k_1 x_1 + \mathrm{i}k_2 x_2 - \mathrm{i}\omega_n(k)t\} \, \mathrm{d}^2\boldsymbol{k}, \tag{2.6}$$

where $a_n(\boldsymbol{k}, t)$ are the modal amplitudes, whose evolution equations are derived in §§ 2.2 and 2.3 of [I]. In the absence of nonlinearity and viscosity, the amplitudes are time independent, but evolve slowly when small nonlinearity and viscosity are allowed for. The interpretation of modes in terms of plane waves provides a length scale $|\boldsymbol{K}|^{-1} = (k^2 + n^2\pi^2)^{-1/2}$ associated with each mode. Going towards smaller scales corresponds to increasing $|\boldsymbol{K}|$ by increasing k or $|n|\pi$, or both.

Given statistical axisymmetry and homogeneity parallel to the walls, the second-order moments of a_n take the form

$$\overline{a_n^*(\boldsymbol{k}, t) a_m(\boldsymbol{k}', t)} = A_{nm}(k, t)\delta(\boldsymbol{k} - \boldsymbol{k}'), \tag{2.7}$$

where A_{nm} is the spectral matrix, which is Hermitian and positive semi-definite. Its diagonal elements represent the energy distributions in $\boldsymbol{k}$-space of the different modal orders, while the off-diagonal ones express correlations between orders. The former, referred to as spectra, are more important than the latter and we focus on the spectra in this article. The non-dimensional energy of the flow is given by (I.3.8) (here and henceforth, (I.x.y) refers to equation (x.y) of [I]) as

$$\frac{1}{2} \sum_{n=-\infty}^{\infty} \int A_{nn}(k) \, \mathrm{d}^2\boldsymbol{k}. \tag{2.8}$$

This is the statistically and x_3-averaged, non-dimensional kinetic energy per unit area of the x_1–x_2 plane. It consists of a sum of contributions from all modes. Note that $A_{-n,-n}(k) = A_{nn}(k)$, so n and $-n$ give equal contributions to the energy. Note also that, because ε is a non-dimensional measure of velocity and A_{nm} expresses second-order velocity moments, $A_{nn} = O(\varepsilon^2)$.

The flow can be expressed as the sum of two components. The first is the combination of all $n = 0$ modes and is referred to as the 2-D component because it is independent of x_3. The second, the wave component, results from the $n \neq 0$ modes. When nonlinearity and viscosity are neglected, the former is steady because $\omega_0(k) = 0$, whereas the latter is oscillatory, each $n \neq 0$ having frequency given by (2.5).

Assuming weak turbulence and small viscous effects, [I] discusses the 2-D component. It is found that evolution occurs on the time scale ε^{-1} and is decoupled from the wave component at leading order. The result is a 2-D flow in which rotation only intervenes via a modification of the pressure variable and a frictional term due to the boundary (Ekman) layers at the walls. Thus, the 2-D part of the flow is as described by the well-established literature (see e.g. the reviews by Kraichnan & Montgomery 1980; Boffetta & Ecke 2012 and the much briefer description by Frisch 1995, § 9.7) on such flows, independently of the wave component. It should be noted that the treatment of the 2-D component in [I]

does not rule out the possibility of significant cumulative effects of waves on the 2-D part over time spans longer than $O(\varepsilon^{-1})$, such as the $O(\varepsilon^{-2})$ we consider. An idea of the analytical complexity involved in investigating this question can be had from Thomas (2016) (in particular his (2.23)), who studied the different, but related, problem of rotating, shallow-water waves. However, in this paper, we focus entirely on the evolution of wave spectra and this question is not addressed.

The wave component involves dispersive waves and is thus open to analysis using wave-turbulence theory. The details of such analysis are given in [I] and it is concluded that, rather surprisingly, the contributions of the 2-D component cancel. This is what allows us to leave the 2-D part to one side and focus on the wave component alone. The end result of the analysis is the evolution equation

$$\frac{\partial A_{nn}(k)}{\partial t} + 2\Re(\Delta_n(k))A_{nn}(k) = \sum_{n_p,n_q\neq 0}\int_{C_{nn_pn_q}(\boldsymbol{k})} \frac{A_{n_pn_p}(p)(\eta_{nn_pn_q}(\boldsymbol{k},\boldsymbol{p})A_{nn}(k) + \lambda_{nn_pn_q}(\boldsymbol{k},\boldsymbol{p})A_{n_qn_q}(|\boldsymbol{k}+\boldsymbol{p}|))}{\Gamma_{n_pn_q}(\boldsymbol{k},\boldsymbol{p})}|\mathrm{d}\boldsymbol{p}|, \tag{2.9}$$

for the wave spectra, $A_{nn}(k)$, $n\neq 0$. Here, the second term on the left-hand side represents viscous energy dissipation and $\Delta_n(k)$ is the complex dissipation coefficient given in [I]. On the other hand, the right-hand of (2.9) expresses nonlinear interactions between different modes and requires further explanation, given below. Because, as noted earlier, $A_{nn} = O(\varepsilon^2)$, the nonlinear time scale for evolution is $O(\varepsilon^{-2})$, a scale which is typical of wave turbulence with quadratic nonlinearity.

The mode, indexed by $\boldsymbol{k}$ and n, whose spectral evolution is described by (2.9), interacts with two others, $(\boldsymbol{p}, n_p)$ and $(\boldsymbol{q}, n_q)$. As usual in spectral theory, for problems, such as the present one, in which nonlinearity is quadratic, such interactions respect the triadic constraint $\boldsymbol{k}+\boldsymbol{p}+\boldsymbol{q}=0$, hence $\boldsymbol{q}=-\boldsymbol{k}-\boldsymbol{p}$, explaining the appearance of $A_{n_qn_q}(|\boldsymbol{k}+\boldsymbol{p}|)$. Allowing for all triads yields the sum over n_p and n_q, as well as the integral over $\boldsymbol{p}$, but, as noted above, the net contribution of the 2-D mode is zero, hence the exclusion of the $n_p=0$ and $n_q=0$ terms in the sum of (2.9). The quantities $\eta_{nn_pn_q}(\boldsymbol{k},\boldsymbol{p})$, $\lambda_{nn_pn_q}(\boldsymbol{k},\boldsymbol{p})$ and $\Gamma_{n_pn_q}(\boldsymbol{k},\boldsymbol{p})$ are geometrical coefficients whose detailed expressions are given in [I]; $\eta_{nn_pn_q}(\boldsymbol{k},\boldsymbol{p}) = \lambda_{nn_pn_q}(\boldsymbol{k},\boldsymbol{p}) = 0$ unless one of the conditions $n\pm n_p\pm n_q=0$ is met. Thus, terms in the sum in (2.9) (and subsequent equations) which do not satisfy this condition are dropped.

Finally, it is important to understand the meaning of the integral in (2.9). In the wave-turbulence limit, nonlinear interactions between mode triads are dominated by $\boldsymbol{p}$ for which

$$\omega_n(k) + \omega_{n_p}(p) + \omega_{n_q}(|\boldsymbol{k}+\boldsymbol{p}|) = 0, \tag{2.10}$$

is satisfied to $O(\varepsilon^2)$. Equation (2.10) is known as the resonance condition and the combined effects of near resonances are expressed by (2.9), in which the integral is taken along the curve, $C_{nn_pn_q}(\boldsymbol{k})$, in the $\boldsymbol{p}$-plane defined by (2.10). The smaller ε, the less non-resonant interactions contribute and the $\varepsilon\to 0$ limit gives the integral over $C_{nn_pn_q}(\boldsymbol{k})$ of (2.9). The expression resonant manifold is often used in the wave-turbulence literature, but in what follows we prefer the description 'resonance curve' for $C_{nn_pn_q}(\boldsymbol{k})$ to emphasise its one-dimensional nature in the present problem. $C_{nn_pn_q}(\boldsymbol{k})$ may or may not exist depending on the values of n, n_p, n_q and k. When it does not exist, the integral in (2.9) should be interpreted as zero. As we shall see, the appearance/disappearance of resonance curves as

k is varied can have significant consequences for spectral evolution, namely the appearance of discontinuities in the spectra predicted by wave-turbulence theory.

Introducing $O(1)$ scaled spectra using $B_n = \varepsilon^{-2} A_{nn}$ and the scaled time $T = \varepsilon^2 t$, (2.9) becomes

$$\frac{\partial B_n(k)}{\partial T} + 2\varepsilon^{-2}\Re(\Delta_n(k))B_n(k) = \sum_{n_p, n_q \neq 0} \int_{C_{nn_pn_q}(\boldsymbol{k})} \frac{B_{n_p}(p)(\eta_{nn_pn_q}(\boldsymbol{k},\boldsymbol{p})B_n(k) + \lambda_{nn_pn_q}(\boldsymbol{k},\boldsymbol{p})B_{n_q}(|\boldsymbol{k}+\boldsymbol{p}|))}{\Gamma_{n_pn_q}(\boldsymbol{k},\boldsymbol{p})} |\mathrm{d}\boldsymbol{p}|, \tag{2.11}$$

which is the system of equations whose numerical solution provides the results of this article. Using equations (I.2.19) and (I.2.22)

$$2\varepsilon^{-2}\Re(\Delta_n(k)) = \underbrace{\beta_w \frac{(1-\omega_n^2(k))^{1/2}}{\sqrt{2}}\{(1+\omega_n(k))^{3/2} + (1-\omega_n(k))^{3/2}\}}_{\textit{Wall damping}} + \underbrace{\beta_v(k^2+n^2\pi^2)}_{\textit{Volumetric damping}}, \tag{2.12}$$

where $\beta_w = 2\varepsilon^{-2}\, Ek^{1/2}$ and $\beta_v = 2\varepsilon^{-2}\, Ek$. Equation (2.12) shows that viscous dissipation is the sum of two components, both of which are positive. The first is due to the boundary layers at the walls and is characterised by the parameter β_w, while the second represents dissipation throughout the flow and introduces the parameter β_v. The factor multiplying β_w is an increasing function of $k/|n|$ from 0 when $k/|n| = 0$ to $\sqrt{2}$ at infinite $k/|n|$. Thus, while volumetric damping increases with k, owing to the factor $k^2 + n^2\pi^2$, wall damping remains bounded. Since $Ek = (\beta_v/\beta_w)^2$, the small Ekman number used in the derivation of (2.11) requires $\beta_v \ll \beta_w$.

Before going further, a brief overview of the main steps leading to (2.11) is perhaps appropriate. The modal decomposition is used because we want to investigate the weak-turbulence limit. Given this limit, the effects of the 2-D component on the wave one is negligible and we focus attention on the wave modes. Nonlinear interactions between wave modes are dominated by near resonances because the turbulence is weak. More precisely, significant interactions require that the resonance condition, (2.10), is satisfied to $O(\varepsilon^2)$. The weak-turbulence assumption of a small Rossby number, $\varepsilon = u'/(2\Omega h)$, implies that only near resonances are important, hence the reduction to a line integral in (2.11).

The initial ($T = 0$) spectra used in the numerical calculation are chosen to be

$$B_n(k) = C \exp\left(-\frac{k^2 + n^2\pi^2}{\Xi^2}\right), \tag{2.13}$$

where $\Xi > 0$ is a parameter defining the spectral width. The idea behind this choice is to start with just the large scales of turbulence and study how smaller scales develop from there, an idea which has a long history and was originally motivated by attempts to model grid turbulence using the Taylor' hypothesis. In this view, the precise form of the initial spectrum is unimportant, just that it concentrates energy in the large scales. The form used here has become traditional in the turbulence community. It seems to have its origin in the seminal work of Orszag on DNS.

Up to now the Rossby number, ε, has only been used in an order-of-magnitude sense. From here on, we choose to define it precisely such that the wave energy, given by (2.8) without the $n = 0$ term, is initially equal to ε^2. Since $A_{-n,-n}(k) = A_{nn}(k)$, this means that

$$\sum_{n=1}^{\infty} \int B_n(k)\, \mathrm{d}^2\boldsymbol{k} = 1. \tag{2.14}$$

Evaluating the integrals in (2.14) using (2.13)

$$C = \frac{1}{\pi \Xi^2 \sum_{n=1}^{\infty} \exp(-n^2\pi^2/\Xi^2)}. \tag{2.15}$$

The problem to be solved consists of (2.11) with (2.12) and the initial spectra (2.13) with (2.15). It has three parameters, namely Ξ, β_w and β_v. Here, Ξ^{-1} describes the size of the large scales of the initial turbulence relative to the channel width. When $\Xi = O(1)$, as we have in mind, the two are comparable, while increasing Ξ makes the large scales smaller and decreasing Ξ increases their size. As noted above, small Ek implies $\beta_v \ll \beta_w$. Furthermore, to stop the dissipative term in (2.11) from killing the turbulence before nonlinearity intervenes, β_w should be $O(1)$ or smaller. Hence, the dissipation parameters are constrained by $\beta_v \ll \beta_w \leq O(1)$. This is the case for all the results given later. Once β_w and β_v have been chosen, the Ekman number follows from $Ek = (\beta_v/\beta_w)^2$. Note that, although β_v is small, the volumetric term in (2.12) increases with k, leading to a dissipative range at large enough k, as in classical turbulence theory. However, as noted earlier, wall damping remains bounded and saps energy at all scales.

3. Numerical implementation

Since $B_{-n}(k) = B_n(k)$, we restrict attention to $n > 0$. Equation (2.11) implies

$$\frac{\partial B_n}{\partial T} = \alpha_n B_n + \tau_n \quad n > 0, \tag{3.1}$$

where, using (2.12),

$$\alpha_n = J_n - \beta_w \frac{(1-\omega_n^2(k))^{1/2}}{\sqrt{2}}\{(1+\omega_n(k))^{3/2} + (1-\omega_n(k))^{3/2}\} - \beta_v(k^2 + n^2\pi^2), \tag{3.2}$$

$$J_n(k) = \sum_{n_p, n_q \neq 0} \oint_{C_{nn_pn_q}(\boldsymbol{k})} \frac{\eta_{nn_pn_q}(\boldsymbol{k},\boldsymbol{p}) B_{|n_p|}(p)}{\Gamma_{n_pn_q}(\boldsymbol{k},\boldsymbol{p})} |\mathrm{d}\boldsymbol{p}|, \tag{3.3}$$

$$\tau_n(k) = \sum_{n_p, n_q \neq 0} \oint_{C_{nn_pn_q}(\boldsymbol{k})} \frac{\lambda_{nn_pn_q}(\boldsymbol{k},\boldsymbol{p}) B_{|n_p|}(p) B_{|n_q|}(|\boldsymbol{k}+\boldsymbol{p}|)}{\Gamma_{n_pn_q}(\boldsymbol{k},\boldsymbol{p})} |\mathrm{d}\boldsymbol{p}|, \tag{3.4}$$

and, as discussed earlier, the sums are restricted to $n \pm n_p \pm n_q = 0$.

3.1. *Calculation of the integrals along the resonance curves*

The main numerical effort in solving (3.1) is the evaluation of the integrals along the resonance curves $C_{nn_pn_q}(\boldsymbol{k})$ in (3.3) and (3.4). Given (2.5) and $n > 0$, there is no solution of (2.10), and hence no resonance curve, if n_p and n_q are positive. When n_p and n_q

are both negative, it can be shown that $C_{nn_pn_q}(\boldsymbol{k})$ exists for all $\boldsymbol{k}$. Finally, when n_p and n_q are of opposite signs, there is a critical value, $k_c(n, n_p, n_q) > 0$, for which the curve exists if $k > k_c$, but not when $k < k_c$. Appendix A describes the method used for the numerical determination of k_c. As $k \searrow k_c$ the curve shrinks down to a point and disappears when $k = k_c$ is crossed. The result is discontinuities in J_n and τ_n as functions of k at $k = k_c(n, n_p, n_q)$ for all n_p and n_q of opposite signs such that $n \pm n_p \pm n_q = 0$, discontinuities which are inherited by B_n following evolution according to (3.1). These discontinuities are a consequence of the wave-turbulence asymptotic limit $\varepsilon \to 0$. When ε is small, but non-zero, we would expect thin regions near $k = k_c$ in which the spectra vary rapidly, rather than being discontinuous (this is analogous to a shock wave in a compressible fluid as the dissipation goes to zero). The present theory does not describe these regions.

Let

$$I_{n_pn_q} = \oint_{C_{nn_pn_q}(\boldsymbol{k})} \frac{\eta_{nn_pn_q}(\boldsymbol{k}, \boldsymbol{p}) B_{|n_p|})(\boldsymbol{k}, \boldsymbol{p})}{\Gamma_{n_pn_q}(\boldsymbol{k}, \boldsymbol{p})} |\mathrm{d}\boldsymbol{p}|, \tag{3.5}$$

denote one of the terms in (3.3). Changing the integration variable to $\boldsymbol{q} = -\boldsymbol{k} - \boldsymbol{p}$ and using $\Gamma_{n_qn_p}(\boldsymbol{k}, \boldsymbol{p}) = \Gamma_{n_pn_q}(\boldsymbol{k}, \boldsymbol{q})$ and the fact that $C_{nn_qn_p}(\boldsymbol{k})$ becomes $C_{nn_pn_q}(\boldsymbol{k})$ in $\boldsymbol{q}$-space

$$I_{n_qn_p} = \oint_{C_{nn_pn_q}(\boldsymbol{k})} \frac{\eta_{nn_qn_p}(\boldsymbol{k}, -\boldsymbol{k} - \boldsymbol{q}) B_{|n_q|}(|\boldsymbol{k} + \boldsymbol{q}|)}{\Gamma_{n_pn_q}(\boldsymbol{k}, \boldsymbol{q})} |\mathrm{d}\boldsymbol{q}|. \tag{3.6}$$

Combining the contributions to the sum of (3.3) from $n_q > n_p$ and $n_q < n_p$ using (3.5) and (3.6), as well as allowing for the special case $n_q = n_p$, (3.3) becomes

$$J_n(k) = \sum_{n_p, n_q} \zeta_{n_pn_q} \oint_{C_{nn_pn_q}(\boldsymbol{k})} \frac{(\eta_{nn_pn_q}(\boldsymbol{k}, \boldsymbol{p}) B_{|n_p|}(p) + \eta_{nn_qn_p}(\boldsymbol{k}, -\boldsymbol{k} - \boldsymbol{p}) B_{|n_q|}(|\boldsymbol{k} + p|))}{\Gamma_{n_pn_q}(\boldsymbol{k}, \boldsymbol{p})} |\mathrm{d}\boldsymbol{p}|. \tag{3.7}$$

Here, $\zeta_{n_pn_q}$ takes the value $1/2$ if $n_p = n_q$ and 1 otherwise, while the sum is over $n_p,\ n_q \neq 0$, $n_q \geq n_p$, $n \pm n_p \pm n_q = 0$. As discussed above, there is no resonance curve when both n_p and n_q are both positive, hence $n_p < 0$, otherwise the integral is zero. Thus, the sum in (3.7) is restricted to n_p and n_q such that $n_p < 0$, $n_q \geq n_p$, $n_q \neq 0$ and one of the conditions $n \pm n_p \pm n_q = 0$ is met. Terms with $n_q > 0$ and $k < k_c$ are zero because the resonance curve does not exist, hence the sum is further restricted to exclude such terms.

Similar reasoning applies to (3.4), but here we have the identities $\lambda_{nn_qn_p}(\boldsymbol{k}, \boldsymbol{p}) = \lambda_{nn_pn_q}(\boldsymbol{k}, \boldsymbol{q})$ and $B_{|n_q|}(p)B_{|n_p|}(|\boldsymbol{k} + \boldsymbol{p}|) = B_{|n_p|}(q)B_{|n_q|}(|\boldsymbol{k} + \boldsymbol{q}|)$, leading to

$$\tau_n(k) = 2 \sum_{n_p, n_q} \zeta_{n_pn_q} \oint_{C_{nn_pn_q}(\boldsymbol{k})} \frac{\lambda_{nn_pn_q}(\boldsymbol{k}, \boldsymbol{p}) B_{|n_p|}(p) B_{|n_q|}(|\boldsymbol{k} + \boldsymbol{p}|)}{\Gamma_{n_pn_q}(\boldsymbol{k}, \boldsymbol{p})} |\mathrm{d}\boldsymbol{p}|, \tag{3.8}$$

with the same restrictions as on the sum in (3.7). Note that, since the spectra are non-negative, as are $\lambda_{nn_pn_q}(\boldsymbol{k}, \boldsymbol{p})$ and $\Gamma_{n_pn_q}(\boldsymbol{k}, \boldsymbol{p})$ according to (I.5.12) and (I.5.14), so is $\tau_n(k)$.

In what follows we choose coordinates such that $k_1 = k$ and $k_2 = 0$. It can be shown that, when it exists, $C_{nn_pn_q}(\boldsymbol{k})$ consists of a single loop which is symmetric under reflexion in the p_1-axis. The curve intersects that axis at two points, namely $p_1 = P^-$ and $p_1 = P^+$, where $P^- < P^+$ correspond to the solutions of (2.10) with $p_2 = 0$. Appendix A describes the numerical determination of $P^\pm$. Figure 3 of [I] shows the resonance curves in the p_1–p_2 plane for different n_p and n_q for the particular case $n = 2$, $k = 3$.

The resonance curves can be described by a differential equation as follows. Let $\sigma(\boldsymbol{p}) = \omega_n(k) + \omega_{n_p}(p) + \omega_{n_q}(|\boldsymbol{k}+\boldsymbol{p}|)$, so the resonance curve is $\sigma(\boldsymbol{p}) = 0$. Since $\sigma(\boldsymbol{p})$ is constant along the curve

$$\boldsymbol{Z} = -\nabla_{\boldsymbol{p}}\sigma = \frac{n_p \pi \boldsymbol{p}}{(p^2 + n_p^2\pi^2)^{3/2}} + \frac{n_q \pi(\boldsymbol{k}+\boldsymbol{p})}{(|\boldsymbol{k}+\boldsymbol{p}|^2 + n_q^2\pi^2)^{3/2}}, \tag{3.9}$$

is a normal vector. Thus, the curve can be described by the differential equation

$$\frac{\mathrm{d}\boldsymbol{p}}{\mathrm{d}s} = (-Z_2, Z_1), \tag{3.10}$$

where s is a parameter. As $p \to \infty$, σ approaches the positive value $\omega_n(k)$. As a result, it is positive outside and negative inside the resonance curve, hence $\nabla_{\boldsymbol{p}}\sigma$ yields an outward normal vector on the curve. It follows from (3.10) and the first equality in (3.9) that increasing s corresponds to traversing the curve in a clockwise sense. Starting at $\boldsymbol{p} = (P^-, 0)$, clockwise motion implies $p_2 > 0$ until $\boldsymbol{p} = (P^+, 0)$ is reached. Continuing the integration, p_2 becomes negative and the remainder of the curve (which is the mirror image of the part in $p_2 > 0$) is traversed until $\boldsymbol{p}$ returns to $(P^-, 0)$. Since the integrands in (3.7) and (3.8) are reflexion symmetric, we focus on the contribution from $p_2 > 0$. The result is multiplied by 2 to obtain the total integral.

On the upper part ($p_2 > 0$) of the resonance curve, let $\boldsymbol{p} = (P^-, 0)$ correspond to $s = 0$ and $s = s_{max} > 0$ to $\boldsymbol{p} = (P^+, 0)$. It follows from (I.5.14), (3.9) and (3.10) that

$$\left|\frac{\mathrm{d}\boldsymbol{p}}{\mathrm{d}s}\right| = \pi \Gamma_{n_p n_q}(\boldsymbol{k}, \boldsymbol{p}), \tag{3.11}$$

hence (3.7) and (3.8) can be expressed as

$$J_n(k) = 2\pi \sum_{n_p, n_q} \zeta_{n_p n_q} \int_0^{s_{max}} (\eta_{n n_p n_q}(\boldsymbol{k}, \boldsymbol{p}) B_{|n_p|}(p) + \eta_{n n_q n_p}(\boldsymbol{k}, -\boldsymbol{k}-\boldsymbol{p}) B_{|n_q|}(|\boldsymbol{k}+\boldsymbol{p}|))\, \mathrm{d}s, \tag{3.12}$$

$$\tau_n(k) = 4\pi \sum_{n_p, n_q} \zeta_{n_p n_q} \int_0^{s_{max}} \lambda_{n n_p n_q}(\boldsymbol{k}, \boldsymbol{p}) B_{|n_p|}(p) B_{|n_q|}(|\boldsymbol{k}+\boldsymbol{p}|)\, \mathrm{d}s, \tag{3.13}$$

where the sums are restricted as described above.

Turning attention to the numerical implementation, $B_n(k)$ is truncated to $0 < n \le n_{max}$ and discretised in k. Truncation means that (3.1) is only applied for $0 < n \le n_{max}$ and the sums in (3.12) and (3.13) are further restricted to $-n_{max} \le n_p,\ n_q \le n_{max}$. Discretisation is carried out as follows. For each $0 < n \le n_{max}$, k takes the values $0 = k_{0,n} < k_{1,n} < \cdots < k_{N_n,n} = k_{max}$. These values are the amalgamation of two sets. The first, $0 = k_0 < k_1 < \cdots < k_N = k_{max}$, does not depend on n and consists of

$$k_i = \chi\left(\exp\left[\frac{i}{N}\ln(1 + k_{max}/\chi)\right] - 1\right) \quad 0 \le i \le N, \tag{3.14}$$

where $\chi > 0$ is a numerical parameter, comparable to the initial spectral width, Ξ. The second varies with n and consists of all $k_c(n, n_p, n_q)$ with the given n and such that the conditions $k_c < k_{max}$, $-n_{max} \le n_p < 0$, $0 < n_q \le n_{max}$ and $n \pm n_p \pm n_q = 0$ are met. Given that we use IEEE double precision, it is highly unlikely that there is coincidence of a critical value with one of (3.14) or with one of the other critical values. To simplify the

program logic, we assume this is the case: each $k_{i,n}$ is either a critical value or one of (3.14), but not both. The spectra are represented by the values of $B_n(k)$ at the discrete k: $B_n^<(k_{i,n})$ and $B_n^>(k_{i,n})$. Apart from the critical $k_{i,n}$, $B_n(k)$ is continuous and $B_n^< = B_n^>$, while, for critical $k_{i,n}$, $B_n^<(k_{i,n})$ denotes the limit as $k \nearrow k_{i,n}$ and $B_n^>(k_{i,n})$ represents $k \searrow k_{i,n}$.

Because of the discontinuities in J_n, τ_n and B_n, care is needed when (3.1) is applied for a critical $k_{i,n} = k_c$. As $k \nearrow k_c$, $J_n(k) \to J_n^<$, $\tau_n(k) \to \tau_n^<$, while $J_n(k) \to J_n^>$, $\tau_n(k) \to \tau_n^>$ as $k \searrow k_c$. Here, $J_n^<$ and $\tau_n^<$ can be calculated using (3.12) and (3.13) at $k = k_c$ without the critical term. It is shown in Appendix B that

$$J_n^> = J_n^< + \frac{2\pi^2}{(\mu_1\mu_2)^{1/2}}(\eta_{nn_pn_q}(\boldsymbol{k}_c, \boldsymbol{p}_c)B_{|n_p|}(p_c) + \eta_{nn_qn_p}(\boldsymbol{k}_c, -\boldsymbol{k}_c - \boldsymbol{p}_c)B_{|n_q|}(|\boldsymbol{k}_c + \boldsymbol{p}_c|)), \tag{3.15}$$

$$\tau_n^> = \tau_n^< + \frac{4\pi^2}{(\mu_1\mu_2)^{1/2}}\lambda_{nn_pn_q}(\boldsymbol{k}_c, \boldsymbol{p}_c)B_{|n_p|}(p_c)B_{|n_q|}(|\boldsymbol{k}_c + \boldsymbol{p}_c|), \tag{3.16}$$

where $\boldsymbol{k}_c = (k_c, 0)$ and $\boldsymbol{p}_c = (p_{1c}, 0)$ is the point to which the critical resonance curve shrinks as $k \searrow k_c$. The determination of p_{1c} is described in Appendix A, while the quantities μ_1 and μ_2 are given by (B4) and (B5).

The integrals in (3.12) and (3.13) are evaluated as follows. Equation (3.10) is integrated numerically using fourth-order Runge–Kutta starting from $s = 0$ and $\boldsymbol{p} = (P^-, 0)$. The step in s is $\Delta s = \delta|\boldsymbol{Z}|^{-1}(P^+ - P^-)$, where δ is a small numerical parameter. The presence of the factor $|\boldsymbol{Z}|^{-1}$ means that Δs varies along the resonance curve and is intended to keep the step in $\boldsymbol{p}$ of approximately constant length, $\delta(P^+ - P^-)$. The factor $P^+ - P^-$ is used to allow for resonance curves which are either large or small in extent. Integration is carried out until $p_2 \le 0$ and the final step length is then refined to make $p_2 = 0$ correct to fourth order in δ. This leads to numerical approximations of s_{max} and P^+, of which the latter can be compared with the value obtained using the method of Appendix A, thus providing a check on accuracy.

At each step in s, the contributions to the integrals in (3.12) and (3.13) are determined and added into running totals which yield numerical approximations to the integrals after the final step. Using (3.9), (3.10) and $n_p < 0$, it can be shown that, as s increases, $q = |\boldsymbol{k} + \boldsymbol{p}|$ increases, while $p = |\boldsymbol{p}|$ is increasing if $n_q > 0$ and decreasing if $n_q < 0$. Thus, given p and q at the start and end of the step, it can be determined if p or q cross one of the discrete values $k_{i,n}$ during the step. If so, the step is divided into subintervals of s, the boundaries between which are the points at which a discrete value is crossed by either p or q. These boundaries are numerically determined by linear interpolation. On the other hand, if there are no crossings, there is just one subinterval, consisting of the entire step. Subintervals with $p > k_{max}$ or $q > k_{max}$ do not contribute to the integrals in (3.12) and (3.13). For all other subintervals, the integrand is evaluated at its midpoint using linear interpolation. Interpolation across the entire step is used for the coefficients $\lambda_{nn_pn_q}(\boldsymbol{k}, \boldsymbol{p})$, $\eta_{nn_pn_q}(\boldsymbol{k}, \boldsymbol{p})$, $\eta_{nn_qn_p}(\boldsymbol{k}, -\boldsymbol{k} - \boldsymbol{p})$, while the spectra are determined by interpolation between the two consecutive discrete values of k which straddle the midpoint of the subinterval. The integrand is multiplied by the extent of the subinterval in s to obtain the contribution to the integral.

3.2. *Time-stepping scheme*

Equations (3.1) and (3.2) describe the time evolution of the spectra and are applied to all discrete k. For $k_{i,n}$ stemming from (3.14), J_n and τ_n are given by (3.12) and (3.13) as is. However, for critical $k_{i,n}$, (3.1) and (3.2) are applied twice: for (a) $k \nearrow k_c$ and (b)

$k \searrow k_c$. The former describes the time evolution of $B_n^<(k_{i,n})$ and uses $J_n^<$ and $\tau_n^<$, which are obtained from (3.12) and (3.13) by omitting the critical term, while the latter uses $J_n^>$ and $\tau_n^>$, given by (3.15) and (3.16). In what follows, we will treat (3.1) as written. However, for critical $k_{i,n}$ it should be borne in mind that, in application a of (3.1), B_n, α_n and τ_n should be interpreted as $B_n^<$, $\alpha_n^<$ and $\tau_n^<$, where $\alpha_n^<$ is given by (3.2) with J_n replaced by $J_n^<$. A similar remark holds for application b.

Time is discretised with step Δ. At each step, there are two stages. In the first, α_n and τ_n are approximated as having the time-independent values α_n^* and τ_n^*, which are calculated using the B_n from the end of the previous time step. This leads to the first approximation

$$B_n^* = \mathrm{e}^{\alpha_n^* \Delta} B_n(T) + \frac{\mathrm{e}^{\alpha_n^* \Delta} - 1}{\alpha_n^*} \tau_n^*, \tag{3.17}$$

of the spectra at the end of the present step, where T is the start of the step. A second approximation is used to improve the order of the scheme. Here, α_n and τ_n take the values α_n^{**} and τ_n^{**}, which are calculated using the spectra $(B_n(T) + B_n^*)/2$. Thus

$$B_n(T + \Delta) = \mathrm{e}^{\alpha_n^{**} \Delta} B_n(T) + \frac{\mathrm{e}^{\alpha_n^{**} \Delta} - 1}{\alpha_n^{**}} \tau_n^{**}, \tag{3.18}$$

completes the time step.

The overall numerical scheme consists of all the approximations described in this and the previous subsection. Discussion of the accuracy of the different elements of the scheme and the scheme as a whole can be found in § 4.8 of Eremin (2019).

4. Results

4.1. *Evolution of the wave energy*

As discussed earlier, the wave energy is represented by the left-hand side of (2.14), i.e.

$$E = \sum_{n=1}^{\infty} \int B_n(k) \, \mathrm{d}^2 \boldsymbol{k}, \tag{4.1}$$

which, allowing for the scaling $B_n = \varepsilon^{-2} A_{nn}$, gives the non-dimensional, statistically and x_3-averaged wave energy per unit area of the x_1–x_2 plane as $\varepsilon^2 E$. Equation (2.14) implies $E = 1$ at the initial time, $T = 0$. An evolution equation for E can be obtained using (2.11). As shown in § 5.5 of [I], the right-hand side of (2.11), representing nonlinear effects, is energy conserving and so does not contribute. This leaves the viscous contribution, hence

$$\frac{\mathrm{d}E}{\mathrm{d}T} = -D_w - D_v, \tag{4.2}$$

where, using (2.12),

$$D_w = \beta_w \sum_{n=1}^{\infty} \int \frac{(1 - \omega_n^2(k))^{1/2}}{\sqrt{2}} \{(1 + \omega_n(k))^{3/2} + (1 - \omega_n(k))^{3/2}\} B_n(k) \, \mathrm{d}^2 \boldsymbol{k}, \tag{4.3}$$

$$D_v = \beta_w \sum_{n=1}^{\infty} \int (k^2 + n^2 \pi^2) B_n(k) \, \mathrm{d}^2 \boldsymbol{k}. \tag{4.4}$$

Here, D_w and D_v are both positive and represent wall and volumetric energy dissipation.

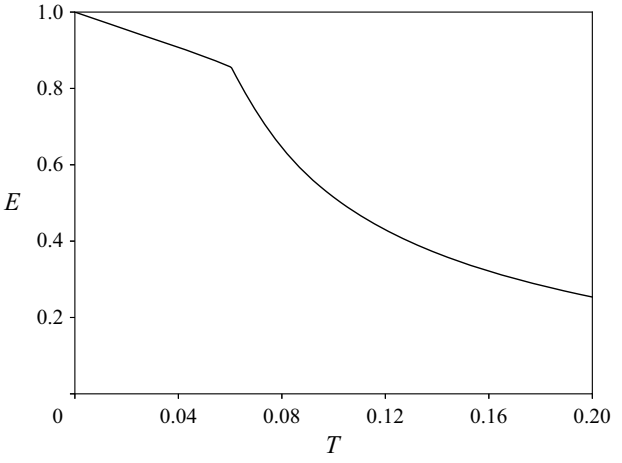

Figure 2. Evolution of the wave energy for $\Xi = 5$, $\beta_w = 2$ and $\beta_v = 0.002$.

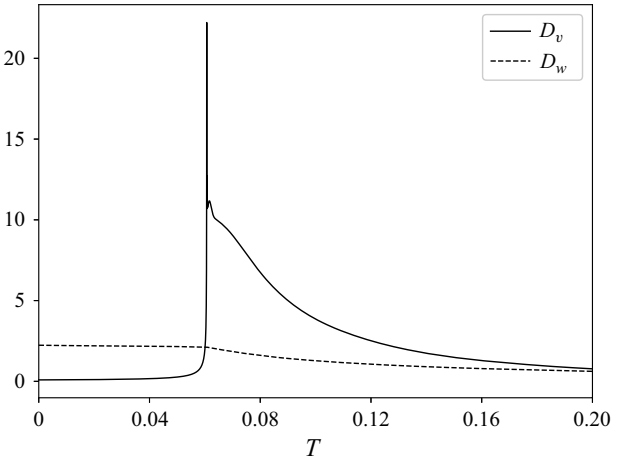

Figure 3. Evolution of D_w and D_v for $\Xi = 5$, $\beta_w = 2$ and $\beta_v = 0.002$.

Figures 2 and 3 show the time evolution of E, D_w and D_v for a particular choice of the parameters Ξ, β_w and β_v. As will be seen from figure 2, there are two phases of evolution. In the first, E decreases, following an approximately linear time dependency. There is then an abrupt transition to more rapid decay. The reason for this behaviour can be seen from figure 3. During the initial phase, wall damping is dominant and D_w is close to constant. However, volumetric damping increases rapidly as a certain time, T_d ($\approx$0.06 in the present case), referred to henceforth as the development time, is approached and it takes over from wall damping as the main dissipative mechanism. As might be expected, and as we shall see later, nonlinearity transfers energy to small scales, leading to the rapid increase in volumetric damping and the formation of a dissipative range of k when T_d is approached. On the other hand, wall damping acts on all scales and so is significant prior to time T_d. Note that the term dissipative range refers to the effects of volumetric damping, not wall damping.

The above results are for the case $\beta_v = 0.002$, a relatively small volumetric damping coefficient. Figure 4 shows the effects of increasing β_v on the evolution of E. The transition

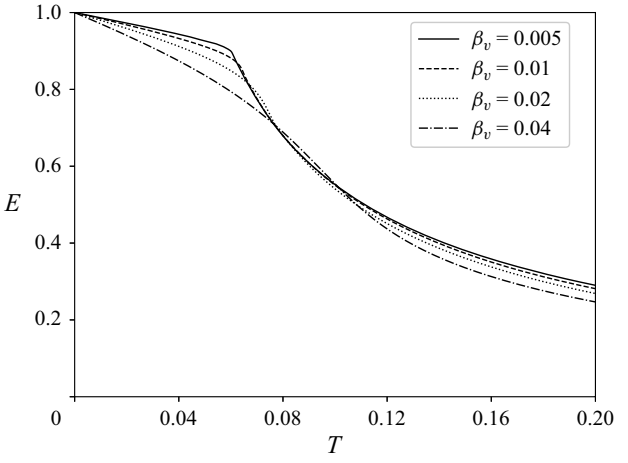

Figure 4. Evolution of the wave energy for $\Xi = 5$, $\beta_w = 1$ and different values of β_v.

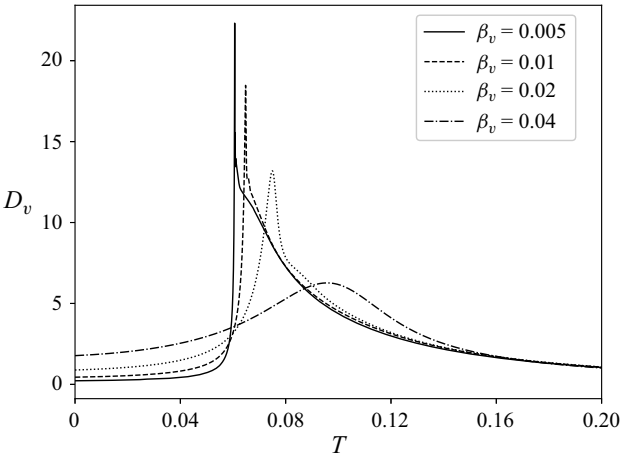

Figure 5. Evolution of D_v for $\Xi = 5$, $\beta_w = 1$ and different values of β_v.

between the two phases of evolution is less and less rapid as β_v increases and takes place at longer times. The latter conclusion may, at first sight, be surprising because one expects the dissipative range to shift to lower k, so less time is needed for its attainment. However, the energy at a given time is reduced by the increased dissipation, which decreases the turbulence intensity. Thus, the nonlinear transfer terms are reduced, leading to slower transfer. And it appears to be this effect which wins.

Figure 5 shows the evolution of D_v for the same parameters as figure 4. The decreasing sharpness of the peak with increasing β_v corresponds to the less rapid transition between the two phases of evolution which was already apparent in figure 4. Given the difficulty of visually identifying T_d for larger values of β_v, we choose to define it using the maximum of D_v.

Table 1 shows values of T_d and $T_d E(T_d)$ for different β_v. The value of $T_d E(T_d)$ is very nearly constant, despite significant variations of T_d. $E(T_d)$ measures the turbulence intensity at time T_d and constancy of $T_d E(T_d)$ supports the suggestion, made above, that the increase in T_d with β_v is due to decreasing turbulence intensity.

β_v	T_d	$T_dE(T_d)$
0.005	0.061	0.0541
0.01	0.065	0.0546
0.02	0.075	0.0551
0.04	0.096	0.0558

Table 1. T_d and $T_dE(T_d)$ for different values of β_v and $\Xi = 5$, $\beta_w = 1$.

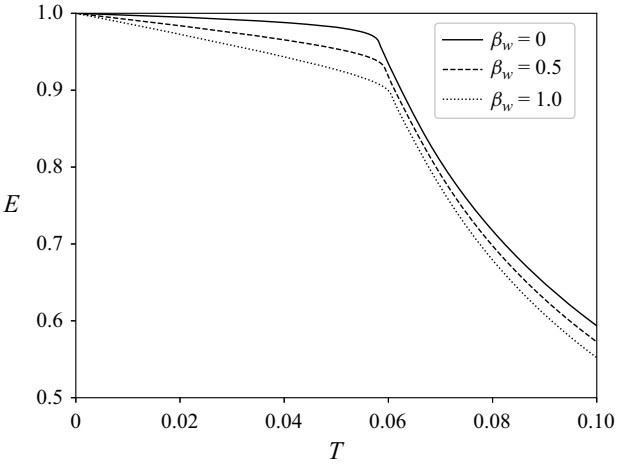

Figure 6. Evolution of the wave energy for $\Xi = 5$, $\beta_v = 0.005$ and different values of β_w.

Figure 6 shows the effects of varying β_w with $\Xi = 5$, $\beta_v = 0.005$, including the case $\beta_w = 0$ in which wall damping is absent. In that case, the energy is not far from constant before $T = T_d$, but nonetheless decreases due to volumetric dissipation. Unsurprisingly, as β_w increases, the energy decays more rapidly in the initial phase, while, following $T = T_d$, it is not greatly affected by β_w.

The value of T_d is shown as a function of β_w for two values of β_v in figure 7. Apparently, it does not depend strongly on either β_w or β_v provided β_v is small enough. It is found to be an increasing function of either of the dissipation coefficients.

Figure 8 shows the evolution of E, D_w and D_v as log–log plots. The straight lines following $T = T_d$ suggest power laws. The slopes of the lines imply exponents -1 for E, -1.02 for D_w and -2.37 for D_v. Note that the exponents of E and D_w are very nearly the same, whereas D_v decays more rapidly. The factor multiplying $B_n(k)$ in the integral of (4.3) is $O(1)$ for all modes and does not weight small scales more than large ones. Thus, like the energy, D_w is dominated by the large scales and it is perhaps not surprising that E and D_w evolve in a similar way. On the other hand, the factor $k^2 + n^2\pi^2$ in (4.4) weights the small scales more than the large ones, so D_v is dominated by the former. It is thus to be expected to have different behaviour. It may be interesting to note that Morize & Moisy (2006) experimentally obtained a temporal exponent of -1 for the energy of confined turbulence at high enough rotation rates. It may also be interesting to observe that -1 is not too far from the value -0.8 obtained by Bellet *et al.* (2006) for the unconfined, homogeneous problem using wave-turbulence theory.

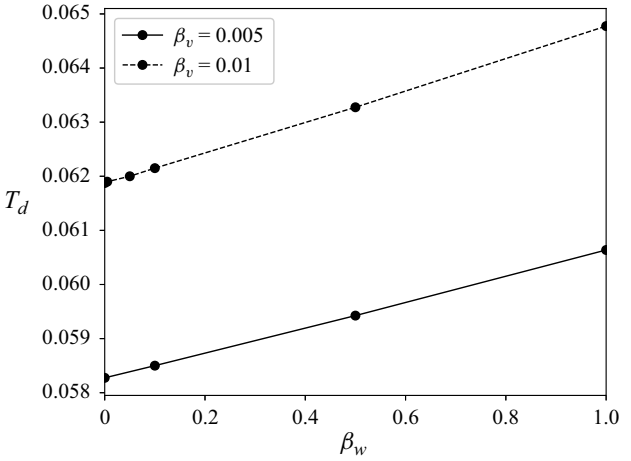

Figure 7. Value of T_d as a function of β_w for $\Xi = 5$ and $\beta_v = 0.005,\ 0.01$.

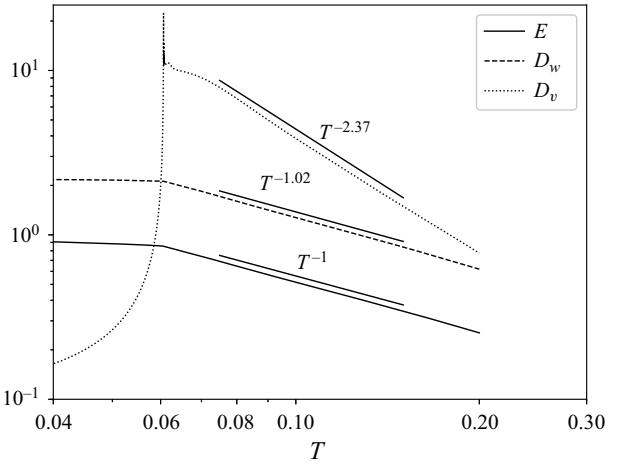

Figure 8. Log–log plots of E, D_w and D_v as a function of T for $\Xi = 5$, $\beta_w = 2$ and $\beta_v = 0.002$.

Having studied the effects of varying β_v and β_w for a single value, $\Xi = 5$, of the spectral width, one can ask the question: How do the results depend on Ξ? Figure 9 shows T_d using a log–log plot as a function of Ξ. It will be seen that T_d is significantly affected by variation of Ξ, decreasing with increasing Ξ. A rough power law of exponent near -2.4 is found at larger Ξ, and perhaps another, of exponent about -0.4, at lower values of Ξ.

4.2. *Spectral evolution*

Initialised using (2.13), the spectra, $B_n(k)$, evolve according to the governing equations, (2.11). This evolution is the subject of this section. As for the overall energy, two phases of evolution are found. Firstly a spectral front propagates towards large k, forming an inertial range behind it. This reflects a transfer of energy to smaller scales. Then, near the development time T_d identified earlier, the spectral advance ceases and a dissipative range is established. In the second phase, the inertial range persists, the spectra decay

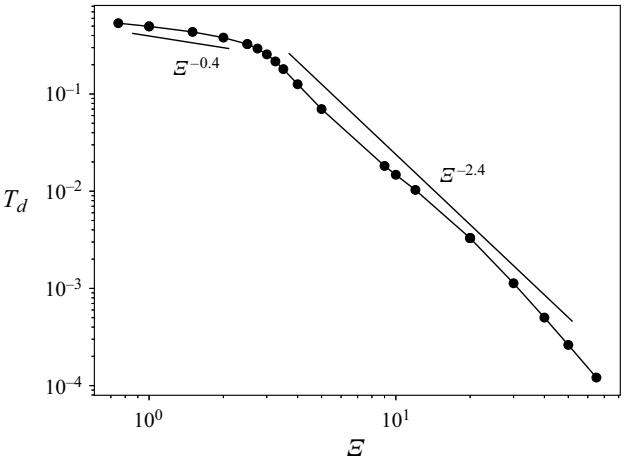

Figure 9. Log–log plot of T_d as a function of Ξ for $\beta_w = 1$ and $\beta_v = 0.01$.

and the dissipative range retreats to smaller k. As expected, spectral discontinuities are encountered.

Figures 10 and 11 show log–log plots of $B_n(k)$ at different times and a particular choice of the parameters Ξ, β_w and β_v. Figure 10 gives results for $n = 1$, $n = 2$ and $n = 6$ at four different times, including $T = 0$ and $T = T_d = 0.0633$, while figure 11 focusses on $n = 1$ and gives results for more values of T. As noted above, there are two evolutionary phases: first a spectral front moves towards larger k. This reflects nonlinear transfer towards smaller scales and forms an inertial range behind the front. This phase lasts until volumetric dissipation becomes important and a dissipative range is established. In the second phase, which begins at the development time, $T_d = 0.0633$ in the present case, the front, now representing the dissipative range, retreats and the spectra decay. There is also nonlinear transfer between different n. This is apparent in the results for $n = 6$ in figure 10, which show increasing B_6 prior to $T = T_d$, followed by decay thereafter. This transfer is found to go from smaller to larger n, i.e. large to small scales (recall that the modal length scale, $(k^2 + n^2\pi^2)^{-1/2}$, decreases as either k or $|n|$ increases). As apparent in plots (c) and (d) of figures 10 and 11, the spectra in the inertial range roughly follow straight lines, indicating approximate power-law dependency on k. As also apparent in figure 11, the front in k accelerates during the first phase of evolution, its rate of advance becoming very large as the development time is approached. This rapid advance of the front near $T = T_d$ is the reason for the sharp onset of volumetric dissipation at small β_v found in the previous section. One might speculate that the front goes to infinite k in a finite time in the absence of volumetric damping. This would explain the insensitivity of T_d to variation of β_v at small enough values. Without volumetric damping, there is nothing to stop energy transfer to infinitely small scales, perhaps generating a singularity at finite time, as found in mathematical studies of the (non-rotating) Euler equations (see e.g. Elgindi & Jeong 2019 and references therein). It may also be of interest to note that, for the unconfined, homogeneous case, Galtier & David (2020, § 5) found a spectral front which goes to infinity at a finite time and a power law corresponding to the $k^{-3.67}$ of figures 10 and 11 prior to the time at which the front reaches infinite k.

Figure 12 shows contour plots of $B_n(k)$ in the k–$n\pi$ plane at different times, the contoured values being the same at all times. These plots illustrate the evolution of the distribution of energy over modes. The first figure reflects the isotropy of the initial

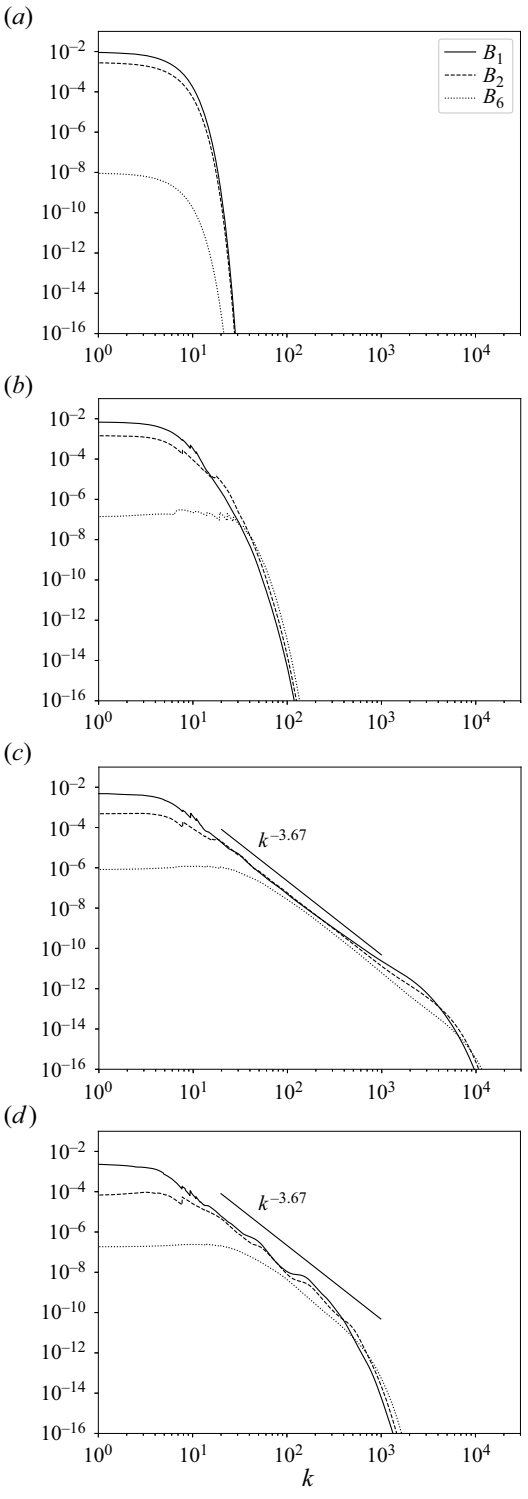

Figure 10. Log–log plots of $B_1(k)$, $B_2(k)$ and $B_6(k)$ for $\Xi = 5$, $\beta_w = 2$ and $\beta_v = 0.005$ at times (*a*) $T = 0$, (*b*) $T = 0.031$, (*c*) $T = 0.0633$ and (*d*) $T = 0.2$. The spectral front advances in (*a*), (*b*), (*c*) and retreats in (*c*), (*d*). The straight lines in (*c*) and (*d*) represent the power law $k^{-3.67}$.

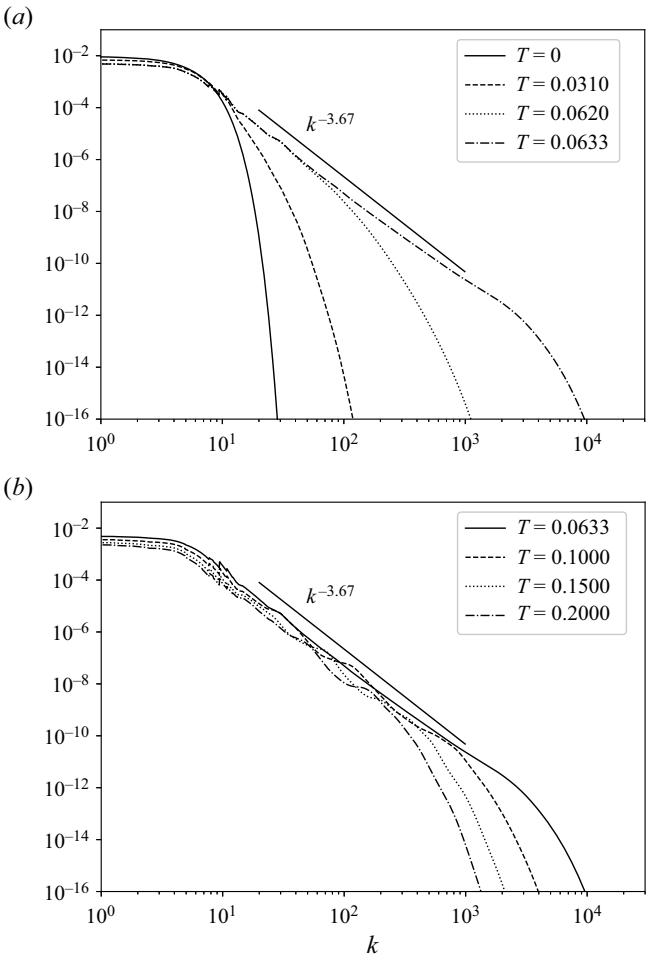

Figure 11. Log–log plots of $B_1(k)$ for $\Xi = 5$, $\beta_w = 2$ and $\beta_v = 0.005$ at different times: (*a*) up to $T = T_d = 0.0633$; (*b*) starting from $T = T_d$. The straight lines represent the power law $k^{-3.67}$.

spectrum, (2.13), and serves as a reference for the other figures. The transfer of energy to smaller scales is reflected by the increased spectral extent at later times. The greater extent in k than in $n\pi$ indicates more efficient transfer in the directions parallel to the walls. It is also apparent that, at and following the development time, for given k, $B_n(k)$ is larger for smaller $n\pi$, having a maximum at $n = 1$. This is not generally true prior to the development time, as shown by the second of figure 12.

Figure 13 illustrates the existence of discontinuities in the spectra. The initial spectra are smooth, but time evolution according to the wave-turbulence closure causes discontinuities to appear, as discussed earlier.

The energy, given by (4.1), can be decomposed in different ways. For instance

$$E = \int_0^\infty e(k)\,\mathrm{d}k, \tag{4.5}$$

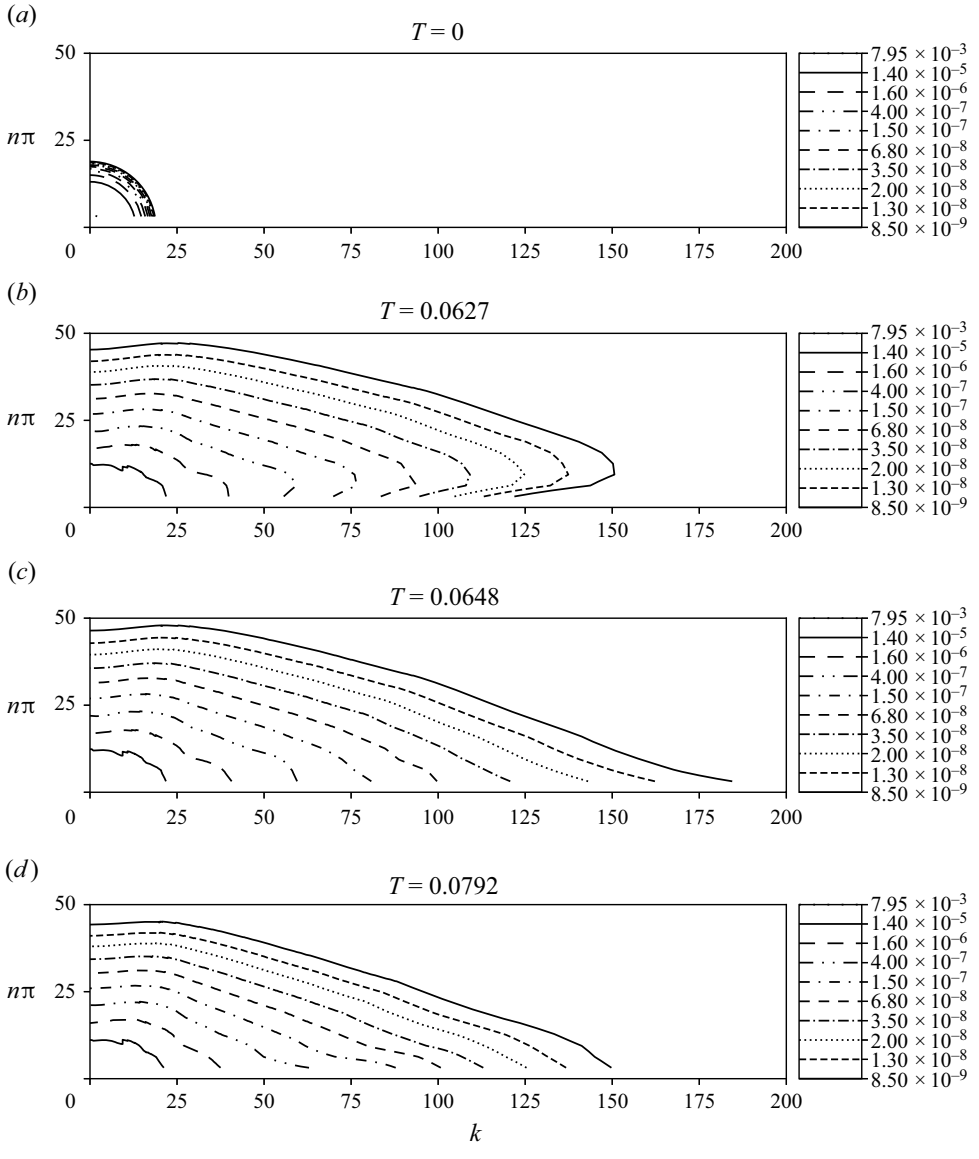

Figure 12. Contour plots of $B_n(k)$ in the k–$n\pi$ plane for $\Xi = 5$, $\beta_w = 1$, $\beta_v = 0.01$ and different values of T, the first of which is at the initial time, the second just prior to $T = T_d$, the third at $T = T_d$ and the fourth at a significantly greater time. The contour values are given on the right-hand side. Of course, the plots only show data for integers $n \geq 1$. Thus, they only extend down to π on the vertical axis.

where

$$e(k) = 2\pi k \sum_{n=1}^{\infty} B_n(k), \tag{4.6}$$

gives the energy distribution over k, and

$$E = \sum_{n=1}^{\infty} e_n, \tag{4.7}$$

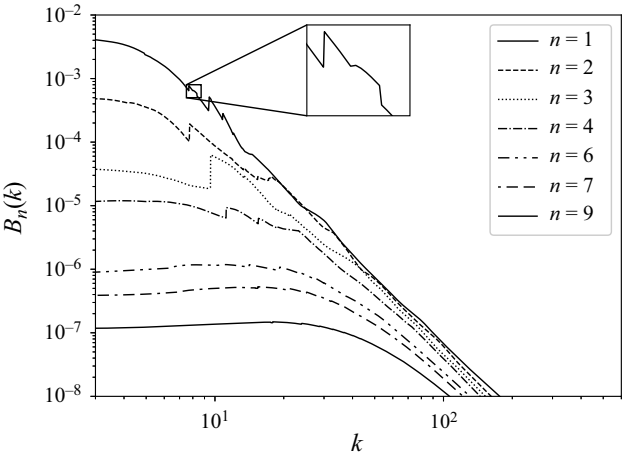

Figure 13. Log–log plots of $B_n(k)$ as a function of k for $\Xi = 5$, $\beta_w = 1$, $\beta_v = 0.01$, different values of n and $T = T_d = 0.0648$.

where

$$e_n = \int B_n(k)\, \mathrm{d}^2\boldsymbol{k}, \tag{4.8}$$

gives the distribution over n. Both distributions are shown in figure 14 for $\Xi = 5$, $\beta_w = 1$ and $\beta_v = 0.01$ and three values of time, including 0 and T_d. These results illustrate the advance, then retreat, of a spectral front in both k and n. They also indicate inertial ranges in k and n to which approximate power laws apply, but with somewhat different exponents for k and n. Figure 15 shows the effects on $e(k)$ at $T = T_d$ of varying β_w and β_v. As might be expected, the main effect is the change in the location of the dissipative range when β_v is varied. The log–log slopes in the inertial range appear to be insensitive to both parameters.

Another measure of turbulence is the spectral flux parallel to the walls. Summing (2.11) over n, multiplying by $2\pi k$, using (4.6) and integrating over k gives

$$\frac{\partial}{\partial T}\int_0^k e(k')\, \mathrm{d}k' = -\Phi(k) - D(k), \tag{4.9}$$

in which the integral is the energy in wavenumbers below k, while the final term expresses dissipation (both volumetric and boundary layer) in the same range. The remaining term, $\Phi(k)$, is the spectral flux across k, which represents nonlinear energy transfer from below to above k. Figure 16 shows $\Phi(k)$ as a function of k for $\Xi = 5$, $\beta_w = 1$ and $\beta_v = 0.01$ at different times, including 0 and T_d. The horizontal axis is logarithmic, while the vertical one is linear. The first thing to note is that the flux is always positive, confirming transfer from small to large scales. The second is that $\Phi(k)$ goes to zero at large k, which reflects the wave-energy conservation by nonlinearity demonstrated in [I]. It can be seen that, consistent with earlier results, there is a significant change in behaviour at the development time. Prior to $T = T_d$, the maximum transfer increases with time and occurs at increasing values of k, while afterwards the converse holds.

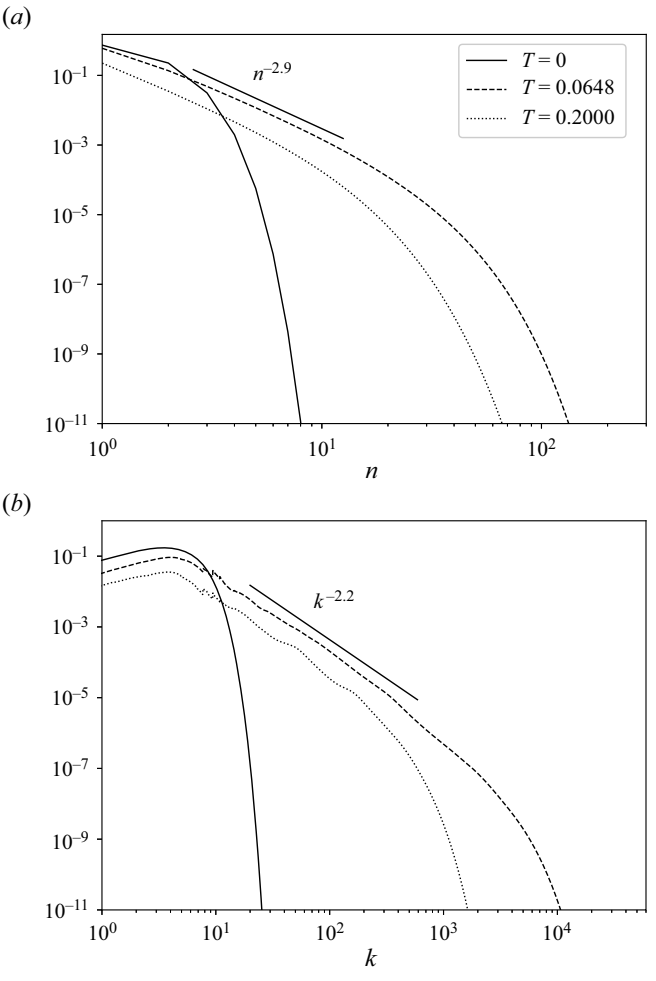

Figure 14. Log–log plots of (*a*) e_n as a function of n and (*b*) $e(k)$ as a function of k for $\Xi = 5$, $\beta_w = 1$ and $\beta_v = 0.01$ at different times.

5. Conclusion

In this paper, we have taken the analytical work of [I] on weak (small Rossby number, ε) turbulence in a rotating channel bounded by infinite parallel walls as a starting point and developed it via numerical implementation to obtain the results given in the previous section. As in [I], spatial coordinates are non-dimensionalised by the channel width and time by $(2\Omega)^{-1}$, where Ω is the rotation rate. In order to stop viscous dissipation from killing the weak turbulence before nonlinearity can intervene, the Ekman number based on the channel width is assumed small.

The analysis is based on the expression of the flow as a combination of modes. Modes are solutions of the linearised, inviscid problem and are indexed by a 2-D wave vector, $\boldsymbol{k}$, and an integer, n, the modal order. The modal amplitudes, $a_n(\boldsymbol{k}, t)$, represent the flow at any given instant of time, t. Modes with $n = 0$ are 2-D, being independent of position across the channel, whereas those with $n \neq 0$ represent inertial waves. Combining all modes with $n = 0$ yields the 2-D component, while the remainder is the wave component.

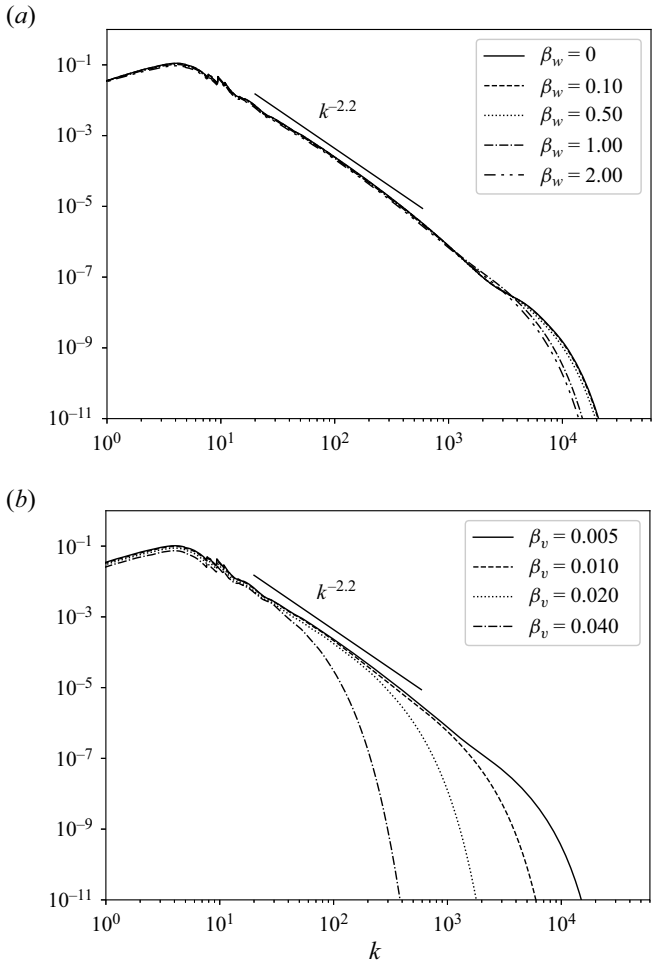

Figure 15. Log–log plots of $e(k)$ for $\Xi = 5$ and $T = T_d$: (*a*) $\beta_v = 0.005$ and different values of β_w; (*b*) $\beta_w = 1$ and different values of β_v.

For small ε, these components are asymptotically decoupled and we have focussed on the wave component.

The flow is assumed statistically axisymmetric and homogeneous in directions parallel to the walls of the channel. The second-order moments of $a_n(\boldsymbol{k})$, yield the spectral matrix $A_{nm}(k)$, where $k = |\boldsymbol{k}|$. The diagonal elements, $A_{nn}(k)$, are referred to as spectra and express the distribution of energy over the different modes. For the weak turbulence studied here, wave-turbulence analysis yields an integro-differential equation which governs the time evolution of $A_{nn}(k)$. Given $A_{nn}(k) = O(\varepsilon^2)$, that equation implies an evolution time of $O(\varepsilon^{-2})$, hence the scaled variables $B_n(k) = \varepsilon^{-2}A_{nn}(k)$ and $T = \varepsilon^2 t$. The wave-turbulence equation, (2.11), is numerically implemented as described in § 3. The initial conditions (2.13) are used and the solution of (2.11) yields the results given in § 4.

The problem has three positive parameters: Ξ, β_w and β_v. Ξ arises from (2.13) and determines the initial spectral width in k–$n\pi$ space, hence the large scales of turbulence are of size $O(\Xi^{-1})$. We have in mind that $\Xi = O(1)$, making the large scales comparable in size to the channel width; β_w and β_v arise from (2.12), which expresses the viscous

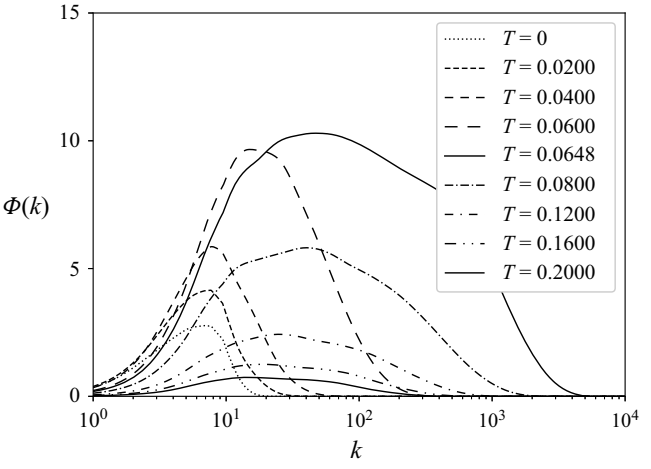

Figure 16. The spectral flux, $\Phi(k)$, as a function of k for $\Xi = 5$, $\beta_w = 1$ and $\beta_v = 0.01$ at different times. The horizontal axis is logarithmic, while the vertical one is linear.

term in (2.11) as the sum of two contributions. One of these represents dissipation due to the wall boundary layers and is characterised by β_w, while the other expresses viscous dissipation throughout the flow (volumetric dissipation) and is characterised by β_v. These parameters are such that $\beta_v \ll \beta_w \leq O(1)$. A mode, $(\boldsymbol{k}, n)$, has an associated length scale $(k^2 + n^2\pi^2)^{-1/2}$. Thus, the volumetric contribution to (2.12), $\beta_v(k^2 + n^2\pi^2)$, increases in importance at small scales. On the other hand, wall dissipation is equally important at all scales. Since $\beta_v \ll \beta_w$, we expect wall dissipation to be dominant for the large scales of turbulence and volumetric dissipation to take over at sufficiently small scales.

There are two main components of the numerical implementation. The first is the calculation of the integrals in (2.11) and is described in § 3.1, while the second is time discretisation, which is the subject of § 3.2. Let us briefly consider the former component. The right-hand side of (2.11) represents nonlinear interactions between modes. Such interactions couple three modes, $(\boldsymbol{k}, n)$, $(\boldsymbol{p}, n_p)$ and $(\boldsymbol{q}, n_q)$ such that $\boldsymbol{k} + \boldsymbol{p} + \boldsymbol{q} = 0$. Thus, given $\boldsymbol{k}$ and varying $\boldsymbol{p}$, $\boldsymbol{q} = -\boldsymbol{k} - \boldsymbol{p}$ determines the third wave vector. Allowing for all modes which interact with $(\boldsymbol{k}, n)$ yields a sum over n_p and n_q and an integral over $\boldsymbol{p}$, as apparent in (2.11). Each mode has an oscillation frequency, denoted $\omega_n(k)$ for mode $(\boldsymbol{k}, n)$. In the wave-turbulence limit, $\varepsilon \to 0$, nonlinear interactions are dominated by mode triads for which the sum of frequencies is zero, a condition expressed by equation (2.10). This equation defines a curve in the $\boldsymbol{p}$-plane denoted $C_{nn_pn_q}(\boldsymbol{k})$ and referred to as the resonance curve. The result is that the integral in (2.11) runs along this curve. The integral is evaluated by taking small steps along the resonance curve and using a numerical approximation for the contribution of each step.

Turning attention to the results, § 4.1 concerns the total wave energy, E, and § 4.2 its distribution over different modes. Most of the results are for the spectral width $\Xi = 5$: only figure 9 concerns other values. Given the scalings used, $E = 1$ at the initial time, $T = 0$. At sufficiently small β_v, the time evolution of E has two distinct phases. In the first, wall dissipation dominates and E has an approximately linear decrease as a function of T. There is then a sharp transition to more rapid decay at a time, T_d, referred to as the development time. As this time is approached, volumetric damping increases rapidly and takes over as the main dissipative mechanism. This is due to transfer of energy to smaller scales, which favours volumetric dissipation.

As β_v increases, the transition between the two phases of evolution becomes less abrupt and takes place at larger T. Given the difficulty of visually identifying the precise temporal location of the transition between evolutionary phases at larger β_v, we chose to define T_d using the maximum of $D_v(T)$, the volumetric dissipation rate.

Varying β_v and β_w, T_d was found to be an increasing function of both parameters. For small enough β_v, it is close to 0.06 for $\Xi = 5$ and insensitive to the choice of β_w. Given that wall damping dominates in the first phase of evolution, increasing β_w leads to faster decay of E during that phase, but has little effect on the second phase.

Log–log plots of E, D_v and D_w as functions of T, where D_v and D_w are the volumetric and wall dissipation rates, suggest approximate power laws for the second phase of evolution. The exponents for E and D_w are near -1 for the parameter values of figure 8, whereas D_v decreases significantly more rapidly. This can be explained as follows. Both E and D_w are dominated by the large scales, whereas D_v arises from small scales, the dissipative range. Thus, it is not surprising that E and D_w behave in a similar way, but that D_v is different. As noted when discussing these results, Morize & Moisy (2006) give an experimentally determined temporal exponent of -1 for confined turbulence at high enough rotation rates, in agreement with our results. We also note that -1 is not too far from the value -0.8 obtained by Bellet *et al.* (2006) for the unconfined, homogeneous problem using wave-turbulence theory.

The value of T_d was found to be significantly affected by variation of Ξ, decreasing as Ξ increases. Two rough power laws appeared for T_d as a function of Ξ, one for lower values of Ξ, the other at larger Ξ.

Section 4.2 gives results for the distribution of energy over different modes. The two phases of evolution described above are again apparent. In the first phase, for given n, a spectral front in $B_n(k)$ as a function of k advances in k. This front represents nonlinear transfer of energy towards smaller scales and leaves behind an inertial range in which the spectra follow approximate power laws. This phase lasts until volumetric dissipation becomes important and a dissipative range is established. In the second phase, which follows the development time, T_d, the front, now representing the dissipative range, retreats and the spectra decay. The front accelerates in the first phase of evolution. The rapid advance of the front as $T = T_d$ is approached is the reason for the sharp onset of volumetric dissipation at small enough β_v. One might speculate that the front goes to infinite k in a finite time in the absence of volumetric damping. This would explain the insensitivity of T_d to variation of β_v at small enough values.

There is also nonlinear transfer towards larger n, i.e. smaller scales. Contour plots of $B_n(k)$ in the k–$n\pi$ plane show energy transfer to small scales in both k and n. They indicate a larger extent in k than in $n\pi$, which means that transfer is more effective parallel to the walls than in the wall-normal direction. They also show that, at or following the development time and for given k, $B_n(k)$ is larger for smaller $n\pi$, having a maximum at $n = 1$.

Although the initial spectra are smooth, discontinuities appear in $B_n(k)$ as a function of k following time evolution. These discontinuities are due to the appearance/disappearance of $C_{nn_pn_q}(\boldsymbol{k})$ as k is varied when n_p and n_q have opposite signs. This causes a jump in the corresponding terms on the right-hand side of (2.11), a jump which is inherited by $B_n(k)$ following evolution. The discontinuities are a consequence of the wave-turbulence asymptotic limit $\varepsilon \to 0$. When ε is small, but non-zero, we would expect thin regions in which the spectra vary rapidly, rather than discontinuities (this is analogous to a shock wave in a compressible fluid as the dissipation goes to zero). The present theory does not describe these regions.

Summing $2\pi k B_n(k)$ over n gives $e(k)$, the distribution of energy over k allowing for all modal orders. Likewise, the distribution, e_n, over n follows from integrating $B_n(k)$ over $\boldsymbol{k}$. Log–log plots of $e(k)$ as a function of k and e_n as a function of n show inertial ranges with approximate power laws.

Finally, the spectral energy flux parallel to the walls was calculated and an example given in figure 16. The results confirm wave-energy conservation, that energy transfer goes from large to small scales and the significant change in behaviour at the development time, $T = T_d$.

Before bringing this article to a close, we should perhaps mention the usual approach (Zakharov *et al.* 1992) for determining the wave-turbulence spectral k-exponent in the inertial range and why it has not been used here. Firstly, rotating turbulence is intrinsically anisotropic, whereas isotropy is a significant ingredient of the Zakharov approach. Secondly, the turbulence is both confined and decaying. Note that, following the development time, the spectral flux in figure 16 is not approximately independent of k in the inertial range, as would be expected in the time-stationary case, and this despite the power law apparent in figure 14(*b*). We see no obvious means of obtaining analytical predictions for the spectral exponents observed in the present case.

Acknowledgements. Thanks to C. Cambon for helpful discussions and suggestions.

Declaration of interests. The authors report no conflict of interest.

Author ORCIDs.
J.F. Scott https://orcid.org/0000-0001-6581-9605;
F.S. Godeferd https://orcid.org/0000-0002-8898-5451.

Appendix A. Determination of k_c, p_{1c} and $P^{\pm}$

We suppose $n > 0$ and n_p and n_q of opposite signs for the determination of $k_c(n, n_p, n_q)$. Since (2.10) is invariant under the transformation $n_p \leftrightarrow n_q, \boldsymbol{p} \leftrightarrow -\boldsymbol{k} - \boldsymbol{p}$, for given n, k_c is unchanged by permutation of n_p and n_q. Thus, we restrict attention to $|n_p| \geq |n_q|$.

Let $\sigma(\boldsymbol{p}) = \omega_n(k) + \omega_{n_p}(p) + \omega_{n_q}(|\boldsymbol{k} + \boldsymbol{p}|)$, which approaches the positive limit $\omega_n(k)$ as $p \to \infty$. The resonance curve, $\sigma(\boldsymbol{p}) = 0$, exists provided the minimum value of $\sigma(\boldsymbol{p})$ is negative. At the minimum, $\nabla_{\boldsymbol{p}}\sigma = 0$, hence

$$\frac{n_p \pi \boldsymbol{p}}{(p^2 + n_p^2\pi^2)^{3/2}} + \frac{n_q \pi (\boldsymbol{k} + \boldsymbol{p})}{(|\boldsymbol{k} + \boldsymbol{p}|^2 + n_q^2\pi^2)^{3/2}} = 0. \tag{A1}$$

Choosing coordinates such that $k_1 = k$ and $k_2 = 0$, (A1) implies $p_2 = 0$ and

$$\frac{n_p \pi p_1}{(p_1^2 + n_p^2\pi^2)^{3/2}} + \frac{n_q \pi (k + p_1)}{((k + p_1)^2 + n_q^2\pi^2)^{3/2}} = 0. \tag{A2}$$

As $k \searrow k_c$, the minimum of $\sigma(\boldsymbol{p})$ approaches zero. Thus, (A2) and

$$\frac{n\pi}{(k^2 + n^2\pi^2)^{1/2}} + \frac{n_p \pi}{(p_1^2 + n_p^2\pi^2)^{1/2}} + \frac{n_q \pi}{((k + p_1)^2 + n_q^2\pi^2)^{1/2}} = 0, \tag{A3}$$

apply when $k = k_c$. Equations (A2) and (A3) provide two equations for the unknowns k_c and p_1. As noted in the main text, the resonance curve shrinks down to a point as $k \searrow k_c$. This point is given by $\boldsymbol{p} = (p_1, 0)$.

Equation (A2) implies

$$27Y^3 - 27Y^2 + 4\gamma = 0, \tag{A4}$$

where

$$Y = \frac{n_q^2\pi^2}{(k+p_1)^2 + n_q^2\pi^2}, \tag{A5}$$

$$\gamma = \frac{27\pi^4 n_p^2 n_q^2 \xi^2}{4(\xi^2 + n_p^2\pi^2)^3}, \tag{A6}$$

and $\xi = |p_1|$. According to (A2), $p_1 \neq 0$, hence $\xi > 0$. Given $|n_p| \geq |n_q|$, it can be shown using (A6) that $0 < \gamma \leq 1$. Equation (A4) has one negative root, which is irrelevant given positivity of (A5). The two others lie in $0 < Y < 1$ and are ordered according to $Y_- \leq Y_+$. Equation (A4) makes the two terms on the left-hand side of (A2) have the same absolute value, but they must also have opposite signs. This condition, and hence (A2), are satisfied by taking

$$k = g_\pm(\xi)\,\mathrm{sgn}(p_1), \tag{A7}$$

where

$$g_\pm(\xi) = -\xi - n_q\pi\,\mathrm{sgn}(n_p)\left(\frac{1-Y_\pm}{Y_\pm}\right)^{1/2}. \tag{A8}$$

Note that $k > 0$, $\xi = |p_1|$ and (A7) imply that

$$k = |g_\pm(\xi)|, \quad p_1 = \xi\,\mathrm{sgn}(g_\pm(\xi)). \tag{A9}$$

Using (A5), (A7) and (A8), (A3) gives

$$h_\pm(\xi) = \frac{n\pi}{(g_\pm(\xi)^2 + n^2\pi^2)^{1/2}} + \frac{n_p\pi}{(\xi^2 + n_p^2\pi^2)^{1/2}} + \frac{n_q\pi}{((g_\pm(\xi)+\xi)^2 + n_q^2\pi^2)^{1/2}} = 0, \tag{A10}$$

whose solutions in $\xi > 0$ yield the critical values via (A9). As $\xi \to 0$, $h_+(\xi) \to \mathrm{sgn}(n_p)$, whereas $h_+(\xi) \to \mathrm{sgn}(n_q)$ as $\xi \to \infty$. Thus, since n_p and n_q have opposite signs, there is at least one solution of $h_+(\xi) = 0$. Equation (A10) was numerically evaluated for n_p and n_q of opposite signs, $0 < n \leq 20$, $|n_q| \leq |n_p| \leq 20$ and ξ taking 10 000 equally spaced values from $\xi = 0$ to $\xi = 200$. For each choice of n, n_p and n_q there was just one change of sign of $h_+(\xi)$ as a function of ξ, while $h_-(\xi)$ never changed sign. These results imply a single value of k_c, obtained from the solution of $h_+(\xi) = 0$ in $\xi > 0$.

In keeping with the above results, for any given n, n_p and n_q such that n_p and n_q have opposite signs, $n > 0$ and $|n_p| \geq |n_q|$, $h_+(\xi)$ is evaluated, starting at $\xi = 0$ and stepping upwards by 1 until it changes sign compared with its value, $\mathrm{sgn}(n_p)$, for $\xi = 0$. This bounds the location of the zero of $h_+(\xi)$ and interval halving is then used to refine ξ. k_c and p_{1c} follow from (A9).

The above procedure requires the solutions $Y_\pm$ of the cubic equation (A4). These are given by

$$Y_+ = \tfrac{2}{3}\sin\tfrac{1}{3}\varphi(\sin\tfrac{1}{3}\varphi + \sqrt{3}\cos\tfrac{1}{3}\varphi), \tag{A11}$$

$$Y_- = 1 - \tfrac{4}{3}\sin^2\tfrac{1}{3}\varphi, \tag{A12}$$

where

$$\sin\varphi = \gamma^{1/2}, \tag{A13}$$

and $0 < \varphi \leq \pi/2$.

The above procedure allows the calculation of $k_c(n, n_p, n_q)$ and $p_{1c}(n, n_p, n_q)$ for all $n > 0$ and n_p and n_q of opposite signs with $|n_p| \geq |n_q|$. $k_c(n, n_p, n_q) = k_c(n, n_q, n_p)$ and $p_{1c}(n, n_p, n_q) = -k_c(n, n_q, n_p) - p_{1c}(n, n_q, n_p)$ give the critical values for $|n_p| < |n_q|$.

Turning attention to the determination of $P^{\pm}$, recall their definition as the points, $\boldsymbol{p} = (P^{\pm}, 0)$, where the resonance curve crosses the p_1-axis. Thus, they are the solutions of (A3). We suppose that $n > 0$ and $n_p < 0$. There are two cases as follows.

(a) When $n_q < 0$, the left-hand side of (A3) is negative when $p_1 = 0$ and positive as $|p_1| \to \infty$. Stepping upwards in p_1 from $p_1 = 0$ in steps of 1 until the left-hand side of (A3) becomes positive leads to an interval containing P^+. The result is then refined by interval halving. A similar procedure is used for P^-.

(b) When $n_q > 0$, there is a critical point characterised by $k = k_c$ and $p_1 = p_{1c} > 0$. With this value of p_1, the left-hand side of (A3) is a decreasing function of k from its value of 0 when $k = k_c$. Thus, the left-hand side of (A3) is negative for $p_1 = p_{1c}$ in the range, $k > k_c$, in which the resonance curve exists. This allows determination of $P^- < p_{1c}$ and $P^+ > p_{1c}$ by stepping in p_1, followed by interval halving.

Appendix B. Derivation of (3.15) and (3.16)

Here, we suppose that $n > 0$ and n_p and n_q have opposite signs, so there exists a critical k_c with associated p_{1c}, and we consider the behaviour of the resulting contributions to $J_n(k)$ and $\tau_n(k)$ as $k \searrow k_c$. Let

$$\sigma(p_1, p_2, k) = \frac{n\pi}{(k^2 + n^2\pi^2)^{1/2}} + \frac{n_p\pi}{(p_1^2 + p_2^2 + n_p^2\pi^2)^{1/2}} + \frac{n_q\pi}{((k + p_1)^2 + p_2^2 + n_q^2\pi^2)^{1/2}}, \tag{B1}$$

then $\sigma = \partial\sigma/\partial p_1 = \partial\sigma/\partial p_2 = 0$ when $k = k_c, p_1 = p_{1c}, p_2 = 0$. Taylor's expansion gives

$$\sigma(p_1, p_2, k) \sim -\kappa(k - k_c) + \tfrac{1}{2}(\mu_1(p_1 - p_{1c})^2 + \mu_2 p_2^2), \tag{B2}$$

where

$$\kappa = -\frac{\partial\sigma}{\partial k}(p_{1c}, 0, k_c), \tag{B3}$$

$$\mu_1 = \frac{\partial^2\sigma}{\partial p_1^2}(p_{1c}, 0, k_c) = \frac{n_p\pi(2p_{c1}^2 - n_p^2\pi^2)}{(p_{c1}^2 + n_p^2\pi^2)^{5/2}} + \frac{n_q\pi(2(k_c + p_{c1})^2 - n_q^2\pi^2)}{((k_c + p_{c1})^2 + n_q^2\pi^2)^{5/2}}, \tag{B4}$$

and

$$\mu_2 = \frac{\partial^2\sigma}{\partial p_2^2}(p_{1c}, 0, k_c) = -\frac{n_p\pi}{(p_{c1}^2 + n_p^2\pi^2)^{3/2}} - \frac{n_q\pi}{((k_c + p_{c1})^2 + n_q^2\pi^2)^{3/2}}, \tag{B5}$$

are found to be positive. Note that we have neglected second-order terms involving $k - k_c$ in (B2). This is because they are small compared with the first term on the right-hand side.

Equation (B2) implies that the resonance curve can be approximated by the small ellipse

$$\mu_1(p_1 - p_{1c})^2 + \mu_2 p_2^2 = 2\kappa(k - k_c). \tag{B6}$$

It also means that (3.10) can be approximated as

$$\frac{\mathrm{d}p_1}{\mathrm{d}s} = \mu_2 p_2, \quad \frac{\mathrm{d}p_2}{\mathrm{d}s} = -\mu_1(p_1 - p_{1c}). \tag{B7a,b}$$

Since $p_2 = 0$ when $s = 0$, the solution of (B7) has the form

$$p_1 = p_{1c} - \mu_2^{1/2} C\cos((\mu_1\mu_2)^{1/2}s), \quad p_2 = \mu_1^{1/2} C\sin((\mu_1\mu_2)^{1/2}s). \tag{B8a,b}$$

As s increases, p_2 first returns to zero when $s = s_{max}$, hence $s_{max} = \pi/(\mu_1\mu_2)^{1/2}$. As $k \searrow k_c$, the resonance curve (B6) shrinks down to the point $\boldsymbol{p}_c = (p_{1c}, 0)$. Thus, the integrands in (3.12) and (3.13) approach their values for $\boldsymbol{k} = \boldsymbol{k}_c$ and $\boldsymbol{p} = \boldsymbol{p}_c$ and are independent of s. Given $s_{max} = \pi/(\mu_1\mu_2)^{1/2}$ and $\zeta_{n_p n_q} = 1$ (because n_p and n_q have opposite signs, hence $n_p \neq n_q$), we obtain (3.15) and (3.16).

References

Bartello, P. 1995 Geostrophic adjustment and inverse cascades in rotating stratified turbulence. *J. Atmos. Sci.* **52**, 4410–4428.

Batchelor, G.K. 1953 *The Theory of Homogeneous Turbulence*. Cambridge University Press.

Bellet, F., Godeferd, F.S., Scott, J.F. & Cambon, C. 2006 Wave turbulence in rapidly rotating flows. *J. Fluid Mech.* **562**, 83–121.

Boffetta, G. & Ecke, R.E. 2012 Two-dimensional turbulence. *Annu. Rev. Fluid Mech.* **44**, 427–451.

Bourouiba, L. 2008 Discreteness and resolution effects in rapidly rotating turbulence. *Phys. Rev. E* **78**, 056309.

Cambon, C. & Jacquin, L. 1989 Spectral approach to non-isotropic turbulence subjected to rotation. *J. Fluid Mech.* **202**, 295–317.

Cambon, C., Mansour, N.N. & Godeferd, F.S. 1997 Energy transfer in rotating turbulence. *J. Fluid Mech.* **337**, 302–332.

Elgindi, T.M. & Jeong, I.-J. 2019 Finite-time singularity formation for strong solutions to the axi-symmetric 3D Euler equations. *Ann. PDE* **5**, 16.

Eresemin, A. 2019 Numerical implementation of the wave-turbulence closure in a rotating channel. PhD thesis, Ecole Centrale de Lyon.

Frisch, U. 1995 *Turbulence*. Cambridge University Press.

Fritts, D.C. & Alexander, M.J. 2003 Gravity wave dynamics and effects in the middle atmosphere. *Rev. Geophys.* **41** (1), 1003.

Galtier, S. 2003 Weak inertial-wave turbulence theory. *Phys. Rev. E* **68**, 015301.

Galtier, S. & David, V. 2020 Inertial/kinetic-Alfvén wave turbulence: a twin problem in the limit of local interactions. *Phys. Rev. Fluids* **5**, 044603.

Godeferd, F.S. & Lollini, L. 1999 Direct numerical simulations of turbulence with confinement and rotation. *J. Fluid Mech.* **393**, 257–308.

Hopfinger, E.J., Browand, F.K. & Gagne, Y. 1982 Turbulence and waves in a rotating tank. *J. Fluid Mech.* **125**, 505–534.

Kartashova, E.A. 1994 Weakly nonlinear theory of finite-size effects in resonators. *Phys. Rev. Lett.* **72**, 2013–2016.

Kim, Y.-J., Eckermann, S.D. & Chun, H.-Y. 2003 An overview of the past, present and future of gravity-wave drag parametrization for numerical climate and weather prediction models. *Atmos. Ocean* **41**, 65–98.

Kraichnan, R.H. & Montgomery, D. 1980 Two-dimensional turbulence. *Rep. Progr. Phys.* **43**, 547–619.

Lvov, Y.V., Nazarenko, S. & Pokorni, B. 2006 Discreteness and its effects on water-wave turbulence. *Physica D* **218**, 24–35.

Monsalve, E., Brunet, M., Gallet, B. & Cortet, P.-P. 2020 Quantitative experimental observation of weak inertial-wave turbulence. *Phys. Rev. Lett.* **125**, 254502.

MORIZE, C. & MOISY, F. 2006 Energy decay of rotating turbulence with confinement effects. *Phys. Fluids* **18** (6), 065107.

MORIZE, C., MOISY, F. & RABAUD, M. 2005 Decaying grid-generated turbulence in a rotating tank. *Phys. Fluids* **17** (9), 095105.

MOUM, J.N. 2021 Variations in ocean mixing from seconds to years. *Annu. Rev. Mar. Sci.* **13**, 201–226.

MÜLLER, P. 1995 Ertel's potential vorticity theorem in physical oceanography. *Rev. Geophys.* **33**, 67–97.

NAZARENKO, S. 2011 *Wave Turbulence*. Springer.

NEWELL, A.C. & RUMPF, B. 2011 Wave turbulence. *Annu. Rev. Fluid Mech.* **43**, 59–78.

PUSHKAREV, A.N. 1999 On the Kolmogorov and frozen turbulence in numerical simulation of capillary waves. *Eur. J. Mech. - B/Fluids* **18**, 345–351.

SAGAUT, P. & CAMBON, C. 2018 *Homogeneous Turbulence Dynamics*, 2nd edn. Springer.

SCOTT, J.F. 2014 Wave turbulence in a rotating channel. *J. Fluid Mech.* **741**, 316–349.

SCOTT, J.F. & CAMBON, C. 2024 Evolution of weak, homogeneous turbulence with rotation and stratification. *J. Fluid Mech.* **979**, A17.

STAPLEHURST, P.J., DAVIDSON, P.A. & DALZIEL, S.B. 2008 Structure formation in homogeneous, freely decaying, rotating turbulence. *J. Fluid Mech.* **598**, 81–103.

TEITELBAUM, T. & MININNI, P.D. 2012 Decay of Batchelor and Saffman rotating turbulence. *Phys. Rev. E* **86**, 066320.

THOMAS, J. 2016 Resonant fast-slow interactions and breakdown of quasi-geostrophy in rotating shallow water. *J. Fluid. Mech.* **788**, 492–520.

THOMAS, J. 2023 Turbulent wave-balance exchanges in the ocean. *Proc. R. Soc. A* **479**, 20220565.

WALEFFE, F. 1993 Inertial transfers in the helical decomposition. *Phys. Fluids* **A5**, 677–685.

ZAKHAROV, V.E., KOROTKEVICH, A.O., PUSHKAREV, A.N. & DYACHENKO, A.I. 2005 Mesoscopic wave turbulence. *JETP Lett.* **82** (8), 487–491.

ZAKHAROV, V.E., L'VOV, V.S. & FALKOVICH, G. 1992 *Kolmogorov Spectra of Turbulence I*. Springer.